Synthesis of Compositionally Defined Single-Crystalline Eu 3+ -Activated Molybdate-Tungstate Solid-Solution Composite Nanowires and Observation of Charge Transfer in a Novel Class...

7 AUTHORS, INCLUDING:

Jinkyu Han
Brookhaven National Laboratory
16 PUBLICATIONS 12 CITATIONS

SEE PROFILE

Coray Mcbean
Stony Brook University
3 PUBLICATIONS 1 CITATION

SEE PROFILE

Lei Wang
Stony Brook University
14 PUBLICATIONS 43 CITATIONS

SEE PROFILE

Haiqing Liu
Stony Brook University
15 PUBLICATIONS 89 CITATIONS

SEE PROFILE

Synthesis of Compositionally Defined Single-Crystalline Eu^{3+}-Activated Molybdate−Tungstate Solid-Solution Composite Nanowires and Observation of Charge Transfer in a Novel Class of 1D CaMoO$_4$−CaWO$_4$:Eu^{3+}−0D CdS/CdSe QD Nanoscale Heterostructures

Jinkyu Han,[†] Coray McBean,[‡] Lei Wang,[‡] Cherno Jaye,[§] Haiqing Liu,[‡] Daniel A. Fischer,[§] and Stanislaus S. Wong*[,†,‡]

[†]Condensed Matter Physics and Materials Sciences Department, Building 480, Brookhaven National Laboratory, Upton, New York 11973, United States

[‡]Department of Chemistry, State University of New York at Stony Brook, Stony Brook, New York 11794-3400, United States

[§]Materials Science and Engineering Laboratory, National Institute of Standards and Technology, Gaithersburg, Maryland 20889, United States

Ⓢ *Supporting Information*

ABSTRACT: As a first step, we have synthesized and optically characterized a systematic series of one-dimensional (1D) single-crystalline Eu^{3+}-activated alkaline-earth metal tungstate/molybdate solid-solution composite CaW$_{1−x}$Mo$_x$O$_4$ (0 ≤ "x" ≤ 1) nanowires of controllable chemical composition using a modified template-directed methodology under ambient room-temperature conditions. Extensive characterization of the resulting nanowires has been performed using X-ray diffraction, electron microscopy, and optical spectroscopy. The crystallite size and single crystallinity of as-prepared 1D CaW$_{1−x}$Mo$_x$O$_4$:Eu^{3+} (0 ≤ "x" ≤ 1) solid-solution composite nanowires increase with increasing Mo component ("x"). We note a clear dependence of luminescence output upon nanowire chemical composition with our 1D CaW$_{1−x}$Mo$_x$O$_4$:Eu^{3+} (0 ≤ "x" ≤ 1) evincing the highest photoluminescence (PL) output at "x" = 0.8, among samples tested. Subsequently, coupled with either zero-dimensional (0D) CdS or CdSe quantum dots (QDs), we successfully synthesized and observed charge transfer processes in 1D CaW$_{1−x}$Mo$_x$O$_4$:Eu^{3+} ("x" = 0.8)−0D QD composite nanoscale heterostructures. Our results show that CaW$_{1−x}$Mo$_x$O$_4$:Eu^{3+} ("x" = 0.8) nanowires give rise to PL quenching when CdSe QDs and CdS QDs are anchored onto the surfaces of 1D CaWO$_4$−CaMoO$_4$:Eu^{3+} nanowires. The observed PL quenching is especially pronounced in CaW$_{1−x}$Mo$_x$O$_4$:Eu^{3+} ("x" = 0.8)−0D CdSe QD heterostructures. Conversely, the PL output and lifetimes of CdSe and CdS QDs within these heterostructures are not noticeably altered as compared with unbound CdSe and CdS QDs. The differences in optical behavior between 1D Eu^{3+} activated tungstate and molybdate solid-solution nanowires and the semiconducting 0D QDs within our heterostructures can be correlated with the relative positions of their conduction and valence energy band levels. We propose that the PL quenching can be attributed to a photoinduced electron transfer process from CaW$_{1−x}$Mo$_x$O$_4$:Eu^{3+} ("x" = 0.8) to both CdSe and CdS QDs, an assertion supported by complementary near edge X-ray absorption fine structure (NEXAFS) spectroscopy measurements.
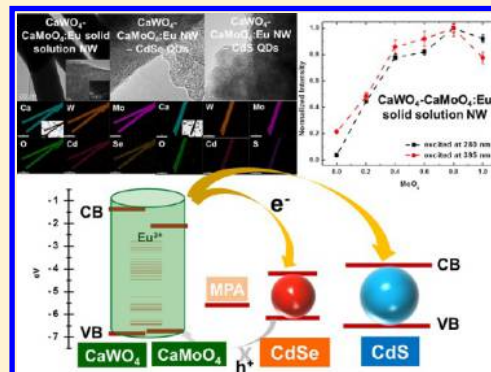
1. INTRODUCTION

Scheelite materials associated with the family of tungstate and molybdate compounds are fundamentally and technologically relevant and significant as a result of their practical usage as components of phosphors, scintillation detectors, gas sensors, optical fibers, laser materials, amplifiers, and photocatalysts.[1−7] In particular, Eu^{3+}-activated CaWO$_4$ and CaMoO$_4$ compounds have drawn significant attention as a new class of luminescent materials, due to their high thermal and chemical stability, relatively strong absorption in the UV to blue range, as well as intense sharp red emission with acceptable color "monochromaticity".[8,9] Specifically, the strong sharp red emission can

be attributed to the f−f transition of Eu^{3+}, which can be significantly enhanced in these scheelite structures by energy transfer from either the WO$_4$$^{2−}$ or MoO$_4$$^{2−}$ group to Eu^{3+} under UV to blue light excitation.[10] Recently, scheelites have become especially attractive as the red emitting components of solid state lighting devices for white light generation, since these materials exhibit favorably broad and intense charge-transfer absorption bands in the near UV or blue region, and therefore

are capable of efficiently capturing the emission from either a GaN- or InGaN-based LED device over a range of wavelengths.[8,9]

Indeed, the optical characteristics (e.g., the emission or excitation peak position and luminescence output) of these luminescent inorganic materials can be potentially further controlled, improved upon, and functionally tuned by structurally altering the host lattice through either cation or anion substitution, which would evidently affect the lattice dimension, the crystallographic symmetry, as well as the electronic band structure of the ultimate composite. In this regard, there have been numerous reports concerning the study and development of interesting luminescence properties in solid-solution compounds including but not limited to a host of interesting semiconducting elemental composite combinations. These have included $ZnS-ZnSe-ZnTe$,[11] $CdSe-CdTe$,[12] and $ZnO-GaN$[13] as well as families of undoped $CaWO_4-CaMoO_4$[14] and $CaWO_4-BaWO_4-SrWO_4$,[15] in addition to rare earth-activated luminescence materials, such as Eu^{2+}-activated $Ba_2SiO_4-Sr_2SiO_4-Ca_2SiO_4$,[16] $Ba_3MgSi_2O_8-Sr_3Mg-Si_2O_8-Ca_3MgSi_2O_8$,[17] and $CaSi_2O_2N_2-SrSi_2O_2N_2$.[18] It is critical to note that the crystal structures of both $CaWO_4$ and $CaMoO_4$ are essentially identical and are described by a tetragonal structure possessing a space group of $I_{41/a}$. In particular, these compounds consist of Ca^{2+} and either WO_4^{2-} or MoO_4^{2-} groups with the corresponding coordination numbers of 8 for metal ions and 4 for either W^{6+} or Mo^{6+}. Hence, it is very reasonable to hypothesize that these two scheelite compounds could indeed form ideal and fully miscible solid-solutions.

To date, various $CaWO_4$ or $CaMoO_4$ possessing different morphologies, such as bulk, zero-dimensional (0D) nanocrystals, as well as one-dimensional (1D) nanotubes and nanowires, have been successfully synthesized using a number of different methods, including sol−gel,[19] molten-salt,[20] hydrothermal,[21] electrospinning,[22] micelle templating,[23] and ultrasonic irradiation protocols.[24] Indeed, research into 1D nanomaterials, such as nanotubes, nanowires, and nanobelts, represents a particularly attractive avenue of work, because 1-D structures are inherently anisotropic, possess shape-dependent properties, and can be easily incorporated into either photonic or nanoelectronic devices.[25−28] In the context of this specific study, our group has already reported on a modified template technique, enabling us to prepare samples of high-aspect-ratio, highly crystalline, and chemically pure $CaWO_4$ nanowires using a facile solution-based U-tube protocol under room temperature and ambient conditions.[15] Indeed, apart from its relative simplicity, flexibility, and generalizability as compared with other synthesis processes, such a reaction can be run in either one or two reaction steps in aqueous solvents, thereby leading to the possibility of high yields with the concomitant formation of little, if any, byproducts.

Nonetheless, it is somewhat surprising that there have not been any methodical efforts to systematically correlate structure through the experimental variable of modulating chemical composition with the corresponding optical properties (e.g., specifically the emission or excitation peak position as well as the luminescence output) of nanoscale 1D Eu^{3+}-activated $CaWO_4-CaMoO_4$ metal oxide solid-solution composite compounds. Therefore, *one key objective* in this Article is that we aim to fundamentally *understand how controlled alterations in the chemical composition* of these Eu^{3+}-activated $CaWO_4$ and $CaMoO_4$ scheelite solid-solution materials within the context of

low-dimensional nanostructure motifs *can yield fundamental insights into structure−property (in this case, optical) correlations*. Therefore, the potential for creating a new and practically relevant family of interesting, optically tunable materials is evident. Specifically, our ability to modulate interactions among constituent molybdates, tungstates, and the corresponding emission centers within discrete solid-solutions of these materials within the context of composite 1D oxide nanomaterials can conceivably contribute to somewhat unpredictable, unforeseen, but nevertheless interesting behavior in the resulting observed absorption, excitation spectra, and luminescence output, respectively.

The *second major and equally important motivating factor* for the current work resides in *the formation of new classes of nanoscale heterostructures*, in this case composed of 1D Eu^{3+}-activated $CaWO_4-CaMoO_4$ metal oxide solid-solutions coupled with different types of 0D semiconducting nanocrystals (QDs), which have not been previously prepared to the best of our knowledge and which represent architectures incorporating optically distinctive and structurally complementary subunits. Nanoscale composites, composed of 0D CdSe QDs attached onto either $CePO_4$:Tb nanowires,[29] $LaPO_4$:Eu^{3+} 1D nanowires, or $LaPO_4$:Eu^{3+} 3D sea-urchin assemblies,[30] represent examples of relevant previous systems we have synthesized over the years. Our work therefore highlights the synthetic potential to rationally design and tailor optical properties and behavior, such as either charge or energy transfer between the two constituent components, within the context of deliberately engineered, complex heterostructures.

Therefore, in this work, on the basis of these nanoscale building blocks (i.e., on the one hand, as-prepared Eu^{3+}-activated $CaWO_4-CaMoO_4$ solid-solution metal oxides and on the other hand, semiconducting CdSe or CdS QDs), we have successfully achieved the synthesis and subsequent optical characterization of 0D QD−1D luminescent rare earth activated scheelite metal oxide architectures. Specifically, we have created not only 1D single-crystalline, stoichiometrically well-defined Eu^{3+}-activated $CaWO_4-CaMoO_4$ solid-solution composites with controllable size and chemical composition but also 0D QD (CdSe or CdS)−1D Eu^{3+}-activated $CaWO_4-CaMoO_4$ heterostructures, thereby combining, taking advantage of, and hopefully moving beyond the inherently intriguing optoelectronic properties of the constituent "precursor" nanomaterials.

To demonstrate this point, we have collected the photoluminescence (PL) excitation and emission spectra, in addition to measuring the corresponding lifetimes of as-prepared nanoscale $CaW_{1-x}Mo_xO_4$:Eu^{3+}−CdSe QD and $CaW_{1-x}Mo_xO_4$:Eu^{3+}−CdS QD heterostructures ($0 \leq$ "x" ≤ 1). In so doing, we have observed PL quenching of $CaW_{1-x}Mo_xO_4$:Eu^{3+} within our CdS and CdSe QD-based heterostructures as compared with unbound $CaW_{1-x}Mo_xO_4$:Eu^{3+}, although we noted little if any significant change in the PL output and lifetimes of the actual CdSe QDs and CdS QDs themselves incorporated as part of our heterostructures. Moreover, the observed PL quenching data of our 1D $CaW_{1-x}Mo_xO_4$:Eu^{3+} in our CdSe QD-based heterostructures are more pronounced as compared with analogous heterostructures created using CdS QDs. We propose therefore that the observed PL quenching of $CaW_{1-x}Mo_xO_4$:Eu^{3+} in our heterostructures can be fundamentally attributed to a differential photoinduced charge (electron) transfer process and

optical response, occurring from $CaW_{1-x}Mo_xO_4{:}Eu^{3+}$ to either CdSe QDs or CdS QDs.

In order to support our hypothesis, we have confirmed the presence of electron transfer from $CaW_{1-x}Mo_xO_4{:}Eu^{3+}$ to either CdSe QDs or CdS QDs within our heterostructure motif by probing the unoccupied states of the conduction band of CdSe QDs, CdS QDs, and $CaW_{1-x}Mo_xO_4{:}Eu^{3+}$, respectively, using near edge X-ray absorption fine structure (NEXAFS) analysis. It is known that X-ray absorption spectroscopy can be used to examine charge (i.e., electron) transfer, since the measured partial electron yield (PEY) intensity is proportional to the unoccupied electronic density of states. Hence, PEY data can provide for direct evidence of electron transfer in our systems.[31−33] As an example of the utility and ubiquity of this technique in analyzing charge transfer within comparable hybrid composites, Wu et al. have reported the presence of charge transfer when probing lithium intercalation into TiS_2 by focusing on the S K-edge in NEXAFS spectra;[31] Chen et al. have utilized both C and N K-edge to probe charge transfer at Cu phthalocyanine−Au(111) interface;[32] and finally, Zhou et al.[33] have observed charge transfer from RuO_2 to carbon nanotubes in RuO_2-coated nanotubes by studying changes in the O K-edge and Ru L_3 edge spectra. With this cumulative set of data at hand therefore, the differential PL quenching and behaviors of both free and "immobilized" $CaW_{1-x}Mo_xO_4{:}Eu^{3+}$, CdSe QDs, and CdS QDs as well as the more pronounced PL quenching of $CaW_{1-x}Mo_xO_4{:}Eu^{3+}$ within the context of QD-based heterostructures have been rationalized in the context of the inherent energy level alignments of $CaW_{1-x}Mo_xO_4{:}Eu^{3+}$, CdSe, and CdS systems, respectively.

2. EXPERIMENTAL SECTION

2.1. Synthesis. *2.1.1. 1D Structures of Eu^{3+}-Activated $CaWO_4$−$CaMoO_4$ Solid-Solution.* The generalized synthesis of 1D $CaWO_4$−$CaMoO_4{:}Eu^{3+}$ solid-solution was accomplished using our U-tube protocol.[15] This procedure takes advantage of an ambient diffusion process involving aqueous solutions of reagents within two hollow glass arms combining with and reacting with each other within the spatial confines of polycarbonate membrane template pores of desired diameter and length. In our experiments, one of the two half cells contained an aqueous solution possessing 0.021 M $CaCl_2$ (99.0%, Alfa Aesar) and 0.004 M $EuCl_3$ (99.99% Alfa Aesar), while the other half cell was filled with $NaMoO_4$ (99.7%, Chem Impex International Inc.) and $NaWO_4$ (99.8%, Chem Impex International Inc.), simultaneously dissolved in aqueous solution. The concentrations of $NaMoO_4$ and $NaWO_4$ were systematically varied, and the ratio of W:Mo was correspondingly altered from 0:1.0, 0.2:0.8, 0.4:0.6, 0.6:0.4, 0.8:0.2, to 1.0:0. The contents of the U-tube apparatus were allowed to mix and intersperse for 24 h in order to allow for full reaction and, hopefully, the complete filling of the template pores with the desired precipitate product. Before drying at 70 °C for 1 h in air, the outer surfaces of the template were abraded and rinsed with deionized water to remove material that had formed outside the spatial confines of the template pores, i.e., bulk precipitate with no regular morphological signature. The template containing as-prepared white nanowires was completely dissolved in chloroform, and subsequently washed several times in order to remove any residual polycarbonate template.

2.1.2. CdSe QD Synthesis. Colloidal and well-crystalline CdSe QDs were prepared using a modification of an existing literature protocol.[34] Specifically, in an inert Ar atmosphere, 158 mg of Se powder (99.5+%, Aldrich Chem Co.) were dissolved in a solution mixture of 1 mL of tributylphosphine (TBP, (95%, Acros Organics)) and 4.2 mL dioctylamine (DOA, (97% Acros Organics)). In a parallel experiment, 25.3 mg of CdO (99%, Acros Organics) and 228 mg of stearic acid (97% Acros Organics) were mixed in a three-necked round-bottom flask and heated to 150 °C, while under stirring in an Ar atmosphere, so as to form a clear yellowish-brown solution. The solution was then allowed to cool, and subsequently, 3.88 g of hexadecylamine (HDA, 90% Acros Organics) and 3.88 g of trioctylphosphine oxide (TOPO, 99% Alfa Aesar) were added to the reaction flask and heated at 320 °C. The reaction flask was purged with Ar, until the reaction was completed. The Se solution was subsequently rapidly injected into the reaction flask at 320 °C, and the reaction was continued for 15 s to enable QD growth. The mixture was later quenched to room temperature, and then washed with aliquots of both CCl_4 and acetone. Acetone was added to the supernatant in order to precipitate the QDs. The isolated TOPO/HDA-capped QDs were stored in hexane at 4 °C, prior to further use.

2.1.3. CdS QD Synthesis. CdS QDs were also synthesized using a modified one-pot protocol.[35] In this case, in a single three-necked round-bottom reaction flask, 53.4 mg cadmium acetate (98%, Alfa Aesar), 91.4 mg myristic acid (99%, Acros Organics), 12.6 mL octadecene (90% Acros Organics), 3.2 mg sulfur (99.999%, Acros Organics), 3.6 mg tetraethylthiuram disulfides (97%, Acros Organics), and 2.0 mg 2,2′-dithiobis-benzothiazole (99%, Sigma-Aldrich) were added, and then the resulting mixture was heated to 120 °C for 2 h under vacuum in order not only to ensure complete solvation of the precursors and initiators but also to promote thorough solution degassing. The mixture was further heated to 240 °C under an inert Ar atmosphere, and subsequent CdS QD growth was accomplished at 240 °C for 40 min. The mixture was later quenched to room temperature, and washed with both acetone and CCl_4. As-prepared, acid-capped CdS QDs were stored in hexane at 4 °C prior to additional processing.

2.1.4. Ligand Exchange of CdS and CdSe QDs and Formation of $CaWO_4$−$CaMoO_4{:}Eu^{3+}$−CdSe and CdS QD-Based Heterostructures. In order to create the desired 0D CdSe/CdS QD−1D $CaWO_4$−$CaMoO_4{:}Eu^{3+}$ heterostructures, we had to perform an initial ligand exchange reaction of our as-prepared QDs so as to eventually coat these QDs with 3-mercaptopropionic acid (MPA, >99%, Sigma-Aldrich). MPA effectively acts as a mediating linker and connector joining QDs with the metal oxides. In effect, because MPA consists of −SH and −COOH as terminal reactive end groups, MPA readily attaches onto CdSe QDs and CdS QDs, which easily and effectively adsorb −SH due to the higher affinity of Cd−S; the unbound −COOH groups in MPA therefore can react with the surfaces of scheelites through favorable electrostatic interactions.[36] Typically, in a suspension of each, 0.04 mmol of TOPO/HDA-capped CdSe QDs and myristic acid-capped CdS QDs were dispersed in 4 mL of hexane, respectively. A solution of 0.1 mmol MPA in 2 mL of methanol (MeOH) was subsequently added dropwise into a stirring dispersion of either CdS QDs or CdSe QDs, respectively. The mixtures were left to stir for 30 min in order to complete the ligand exchange process, enabling transport of the QDs from the nonpolar hexane layer to the polar MeOH layer. The CdSe QDs and CdS QDs were subsequently washed with ethanol and

methanol for several times and then redispersed in acetonitrile prior to later use.

The resulting MPA-capped CdSe QDs and CdS QDs were anchored and immobilized onto 1D nanowires composed of $CaWO_4$–$CaMoO_4$:Eu^{3+} solid-solutions, presumably through electrostatic interactions, in an analogous manner to previous reports of various QDs attached onto relatively simple metal oxides, such as TiO_2 and ZnO.[37,38] In a typical experiment, 1.5 mg of $CaWO_4$–$CaMoO_4$:Eu^{3+} solid-solution nanowires dispersed in 3 mL of acetonitrile was allowed to react with 0.03 mmol MPA-capped CdSe QDs and CdS QDs in 3 mL of acetonitrile. The mixture was sonicated for 10 min, and then stirred overnight in the dark as a precautionary measure in order to ensure and maintain the optical integrity of the QDs. The total volume of acetonitrile was kept at 6 mL for the goal of concentration normalization in order to compare the photoluminescence behavior of as-generated heterostructures with that of the constituent, bare, and unbound CdSe QDs, CdS QDs, and $CaWO_4$–$CaMoO_4$:Eu^{3+}, respectively.

2.2. Characterization. Samples were (i) structurally probed using different complementary microscopy and diffraction techniques, including powder X-ray diffraction (XRD), scanning electron microscopy (SEM), transmission electron microscopy (TEM), energy-dispersive X-ray spectroscopy (EDS), and high resolution TEM (HRTEM). Samples were subsequently (ii) optically probed using UV–vis spectroscopy, steady-state photoluminescence (PL) spectroscopy, and time-resolved fluorescence lifetime spectroscopy as well as with near edge X-ray absorption fine structure (NEXAFS) spectroscopy.

2.2.1. X-ray Diffraction. Crystallographic and purity data on as-prepared $CaW_{1-x}Mo_xO_4$:Eu^{3+} ("x" = 0, 0.2, 0.4, 0.6, 0.8, and 1) were obtained using a Rigaku Ultima III Diffractometer, operating in the Bragg configuration using Cu Kα radiation (1.54 Å). Specifically, diffraction data were collected in a range from 15 to 60°, measured at a scanning rate of 1° per minute. To prepare as-generated 1D $CaWO_4$–$CaMoO_4$:Eu^{3+} nanowires for this analysis, samples were rendered into suspensions, i.e., in ethanol for 1D structures of $CaW_{1-x}Mo_xO_4$:Eu^{3+} ("x" = 0, 0.2, 0.4, 0.6, 0.8, and 1). Samples were subsequently sonicated for about 1 min, and then air-dried upon deposition onto glass slides.

2.2.2. Electron Microscopy. SEM images were obtained at 15 kV on a JEOL 7600F instrument. Low-magnification TEM images were acquired using an accelerating voltage of 120 kV on a JEOL JEM-1400 instrument, equipped with EDS mapping capabilities. HRTEM images coupled with complementary selected area electron diffraction (SAED) patterns were recorded using a JEOL JEM-3000F microscope equipped with a Gatan image filter (GIF) spectrometer operating at an accelerating voltage of 300 kV as well as on a JEOL 2100F analytical TEM instrument, equipped with a Gatan CCD camera and a Gatan HAADF detector, operating at an accelerating voltage of 200 kV. Specimens for all of these characterization experiments were prepared by dispersing the as-prepared nanostructures in ethanol, sonicating for 2 min to ensure their adequate dispersion, and evaporating one drop of the solution onto either (i) a Si wafer for SEM analysis or (iii) a 300 mesh Cu grid, coated with a lacey carbon film, for subsequent TEM and HRTEM analysis.

2.2.3. NEXAFS. Cd $M_{2,3}$-edge and Mo $M_{2,3}$-edge NEXAFS spectra were acquired at the U7A NIST/DOW end station at the National Synchrotron Light Source at Brookhaven National Laboratory. The partial electron yield (PEY) signal was collected using a channeltron electron multiplier equipped with an adjustable entrance grid bias. A variable negative bias in the range 20–200 V was applied to remove the extraneous background due to the presence of low-energy electrons. The use of different biases allowed for both top-surface and bulk (up to 10 nm) analyses. Data were recorded in a UHV chamber at room temperature, with an incident X-ray resolution of 0.2 eV. All spectra shown were processed through standard pre- and post-edge normalization methods. Additional experimental details can be found in previously published work.[39−42]

2.2.4. UV–Vis and Fluorescence Spectroscopy. UV–vis spectra were collected at high resolution on a Thermospectronics UV1 spectrometer using quartz cells possessing a 10 mm path length. Individual spectra were obtained for MPA-capped CdSe and CdS QDs, $CaW_{1-x}Mo_xO_4$:Eu^{3+} nanowires, and their associated heterostructure samples, all of which were individually sonicated for 2 min in ethanol so as to yield a homogeneous dispersion for the duration of the measurement. Samples for PL spectra were dispersed in either MeOH or acetonitrile for measurements of MPA-capped CdSe QDs as well as for CdSe QD/CdS QD–$CaW_{1-x}Mo_xO_4$:Eu^{3+} heterostructures. All of these materials were sonicated for 1 min, prior to data collection.

Fluorescence data were subsequently obtained at room temperature using a FluoroMax-4 spectrofluorimeter (Jobin Yvon) with 5 s integration times, using excitation wavelengths of 280, 300, and 395 nm, respectively. The corresponding fluorescence lifetimes were measured with a FluoroMax-4 spectrofluorimeter equipped with both an IBH NanoLED, emitting at 388 nm as an excitation source, and a NanoLED controller module, Fluorohub (Jobin Yvon), operating at 1 MHz. Relevant decay data analysis and interpretation was enabled using the DAS6 software (Horiba Jobin Yvon IBH).

3. RESULTS AND DISCUSSION

3.1. Structural Insights into Eu^{3+}-Activated 1D $CaW_{1-x}Mo_xO_4$ ($0 \leq$ "x" ≤ 1) Nanowires. The purity and crystallinity of our Eu^{3+}-activated $CaW_{1-x}Mo_xO_4$ ($0 \leq$ "x" ≤ 1) 1D nanowires were initially characterized using XRD. The XRD patterns suggest that our as-synthesized metal tungstate–molybdate solid-solution compound is composed of a single tetragonal scheelite structure with a space group of $I_{41/a}$, which agrees well with the JCPDS 72-1624 database standard for "x" = 0 and JCPDS 29-0351 database standard for "x" = 1, as shown in Figure 1. We should note that Eu^{3+} dopants have little influence on the crystal structure of the underlying host lattice, due to the comparable ionic sizes of Ca^{2+} (0.112 nm) and Eu^{3+} (0.110 nm), a finding consistent with prior reports.[43,44] The structure of $CaW_{1-x}Mo_xO_4$ represents the prototype of typical scheelites including but not limited to $MgWO_4$, $CaMoO_4$, $PbMoO_4$, $PbWO_4$, and $YLiF_4$, and consists of Ca^{2+} ions coupled with either WO_4^{2-} or MoO_4^{2-} groups, possessing the corresponding coordination numbers of 8 for Ca^{2+} and 4 for either W^{6+} or Mo^{6+}, respectively, as shown in Supporting Information Figure S1.[45,46]

Interestingly, the constituent crystallite size, as estimated by the Debye–Scherrer formula, increases with increasing "x" and is found to be 12.4, 14.8, 13.6, 16.7, 18.7, and 38.9 nm for "x" = 0, 0.2, 0.4, 0.6, 0.8, and 1, respectively. This variation can be mainly associated with the differential growth rate (or diffusion rate) of molybdenum and tungsten in 1D nanowires. On the basis of the Lifshitz–Slyozov–Wagner[47] and Stokes–Einstein
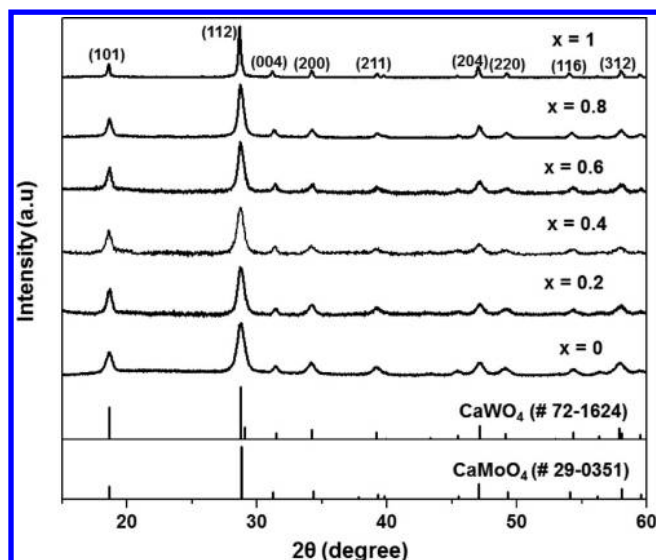
Figure 1. XRD patterns of as-prepared 1D $CaW_{1-x}Mo_xO_4:Eu^{3+}$ ("x" = 0, 0.2, 0.4, 0.6, 0.8, and 1) nanowires. The corresponding JCPDS 72-1624 and 29-0351 database standard values for bulk $CaWO_4$ and $CaMoO_4$, respectively, are also shown below as a comparison.

equations,[48] the average radii (and hence, an indirect measure of the average crystal growth rate) of our as-prepared materials should be inversely proportional to their molecular weight (i.e., R^3 is proportional to D and D is proportional to $M^{-1/3}$, where R = the average radius of all particles, D = the diffusion coefficient, and M = the molecular weight) under identical reaction temperature and time conditions. In our protocols, all samples were prepared under the same reaction parameter space of temperature (RT) and time. However, because the molecular weight of Mo (95.94 g/mol) is smaller than that of W (183.84 g/mol), the reaction and diffusion rates for the fabrication of $CaMoO_4:Eu^{3+}$ nanowires were likely faster than those of $CaWO_4:Eu^{3+}$, an assertion which would lead to the expectation and subsequent observation of a larger crystallite size of $CaMoO_4:Eu^{3+}$ (when "x" = 1) as compared with that of $CaWO_4:Eu^{3+}$ (when "x" = 0).

When probing the behavior of possible peak shifts in the actual diffraction data of $CaW_{1-x}Mo_xO_4:Eu^{3+}$, we generally observed a dependence on "x", as expected. That is, while the XRD patterns of the series' "book ends" of $CaWO_4$ (JCPDS 72-1624) and $CaMoO_4$ (JCPDS 29-0351), respectively, are not noticeably different, as shown in Figure 1, it can be clearly observed that the (004) and (200) peaks corresponding to the scheelite structure do in fact shift to lower and higher scattering
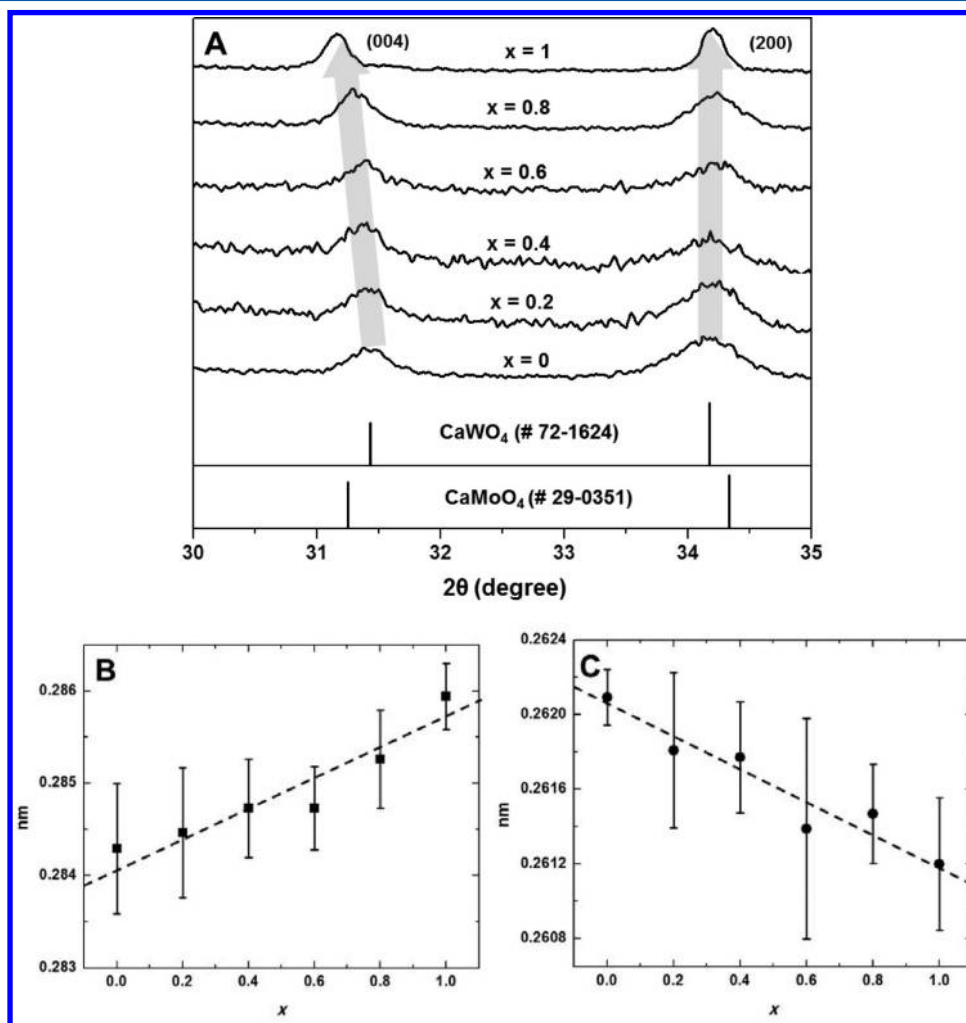

Figure 2. (A) XRD patterns of as-prepared $CaW_{1-x}Mo_xO_4:Eu^{3+}$ ("x" = 0, 0.2, 0.4, 0.6, 0.8, and 1) nanowires in the range of 2θ of 30−35° and the corresponding d spacing behavior of both (B) (004) and (C) (200) lattice planes, plotted as a function of "x".
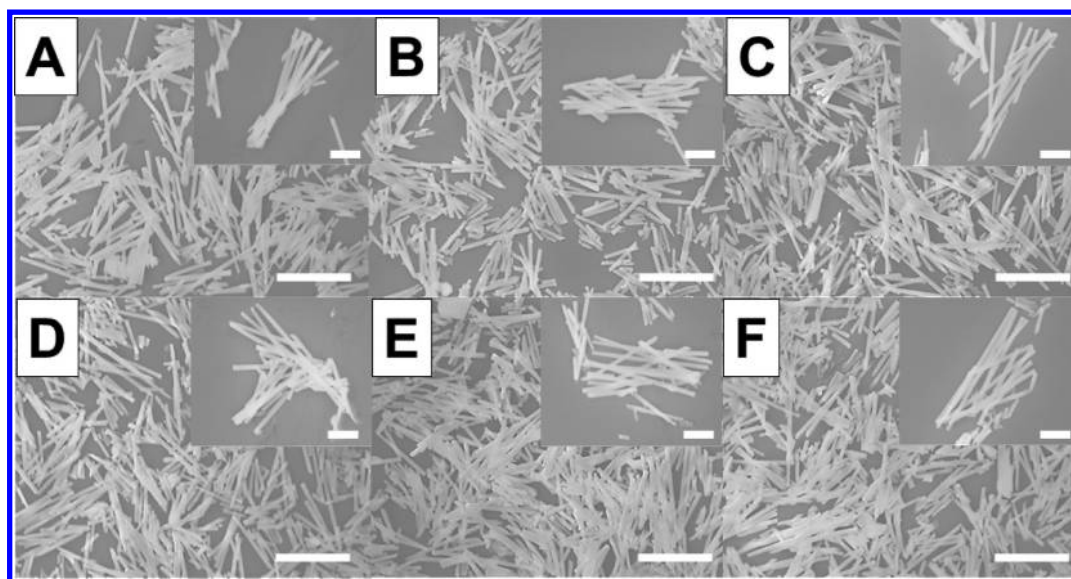
Figure 3. SEM images of as-prepared nanowires of 1D $CaW_{1-x}Mo_xO_4$:Eu^{3+}, where (A) "x" = 0, (B) "x" = 0.2, (C) "x" = 0.4, (D) "x" = 0.6, (E) "x" = 0.8, and (F) "x" = 1. Insets to parts A−F, respectively, represent the corresponding SEM images obtained at higher magnifications. Scale bars in the main figures and corresponding insets in every image are 5 and 2 μm, respectively.

angles, respectively, in the region of 2θ = 30−35°, as "x" increases, as shown in Figure 2A. In other words, the (004) and (200) planes corresponding to the tetragonal phase of $CaWO_4$ are gradually transformed into the analogous peaks of $CaMoO_4$, as "x" increases, as expected. On the basis of several measurements of the diffraction patterns, the average peak positions we obtained for (004) peaks of all samples were located at 2θ = 31.43° ± 0.08°, 31.41° ± 0.08°, 31.38° ± 0.06°, 31.38° ± 0.04°, 31.32° ± 0.06°, and 31.26° ± 0.04° for "x" = 0, 0.2, 0.4, 0.6, 0.8, and 1, respectively. The corresponding positions of the (200) peaks were found at 2θ = 34.17° ± 0.02°, 34.20° ± 0.06°, 34.21° ± 0.04°, 34.25° ± 0.08°, 34.26° ± 0.04°, and 34.27° ± 0.04° for "x" = 0, 0.2, 0.4, 0.6, 0.8, and 1, respectively.

The analogous behavior of the d spacing values of (004) and (200) planes as a function of "x" is shown in Figure 2B and 2C, respectively. The d spacings of (004) and (200) planes varied effectively linearly with composition change, as shown in Figure 2B and 2C, respectively, and are in agreement with Vegard's law. These data collectively and unambiguously indicate that our 1D $CaW_{1-x}Mo_xO_4$:Eu^{3+} nanowires are likely to be essentially "ideal" and uniform solid-solutions, since neither an apparent phase separation nor an obvious separate nucleation of either $CaWO_4$ or $CaMoO_4$ was observed in our solid-state solution compounds.

3.2. Size, Structure, and Morphology of 1D Ca-($W_{1-x}Mo_x$)O_4:Eu^{3+} Nanostructures. The size, structure, and morphology of 1D structural motifs of $CaW_{1-x}Mo_xO_4$:Eu^{3+} (0 ≤ "x" ≤ 1) have been investigated using data acquired from SEM, TEM, HRTEM, and selected area electron diffraction (SAED) patterns. Typical SEM images of 1D $CaW_{1-x}Mo_xO_4$:Eu^{3+} ("x" = 0, 0.2, 0.4, 0.6, 0.8, and 1) nanowires are shown in Figure 3A−F, respectively. The magnitudes of the sizes of our as-prepared $CaW_{1-x}Mo_xO_4$:Eu^{3+} ("x" = 0, 0.2, 0.4, 0.6, 0.8, and 1) nanowires do not noticeably depend upon "x". On the basis of the statistical measurements of several tens of nanowires pertaining to each of our samples, our nanowires in effect measure on average 310 ± 32 nm in diameter with lengths of 4.05 ± 1.60 μm. We should note that

the final morphology of each product accurately replicated the internal pore structure, imperfections, and corresponding morphology of the originating polycarbonate template membranes, and this recurring 1-D motif was found to be independent of the chemical composition of the corresponding $CaW_{1-x}Mo_xO_4$:Eu^{3+} solid-solutions, as expected.

In order to obtain additional insight into the nature of the morphology and crystallographic structure of 1D Eu^{3+}-activated $CaW_{1-x}Mo_xO_4$ solid-solution systems, as-prepared 1D nanowire samples were further examined by both regular TEM and HRTEM imaging as well as with SAED patterns. Figure 4 displays representative TEM images, HRTEM images, and SAED patterns, acquired on $CaW_{1-x}Mo_xO_4$:Eu^{3+} ("x" = 0, 0.2, 0.4, 0.6, 0.8, and 1), respectively. It can be clearly observed that all of the products (Figure 4A−C and G−I), prepared using the 200 nm diameter pore sizes of the PC membranes, mainly consist of discrete and filled one-dimensional nanowires possessing smooth outer surfaces and that their as-prepared dimensions measure ∼300 nm and 4 μm in terms of diameter and length, respectively. These data are consistent with results acquired from the SEM images in Figure 3. Furthermore, the expected elements (i.e., Ca, Mo, and W) present in the solid-solution nanowires are uniformly distributed within the nanowires, as confirmed by complementary EDS spectra (Supporting Information Figure S2), thereby implying that our synthetic protocols successfully produce highly chemically homogeneous solid-solution nanowires. Moreover, HRTEM revealed interlayer spacings, corresponding to the expected lattice parameters associated with the tetragonal scheelite structure of $CaW_{1-x}Mo_xO_4$:Eu^{3+} ("x" = 0, 0.2, 0.4, 0.6, 0.8, and 1), as shown in Figure 4D−F and 4J−L, respectively. Measured interplanar spacings estimated to be about 0.230, 0.262, 0.310, and 0.476 nm could be ascribed to the (211), (200), (112), and (101) lattice planes, respectively. The associated electron diffraction patterns (insets) can be indexed to the reflection of a pure body-centered tetragonal $CaW_{1-x}Mo_xO_4$:Eu^{3+} (i.e., "x" = 0, 0.2, 0.4, 0.6, 0.8, and 1) scheelite structure.

In addition, surprisingly, the observed polycrystallinity in our $CaW_{1-x}Mo_xO_4$:Eu^{3+} nanowires gradually evolved into a more

Figure 4. Representative TEM and HRTEM images of as-prepared nanowires of 1D $CaW_{1-x}Mo_xO_4$:Eu^{3+}: (A and D) "x" = 0, (B and E) "x" = 0.2, (C and F) "x" = 0.4, (G and J) "x" = 0.6, (H and K) "x" = 0.8, and (I and L) "x" = 1, respectively. Corresponding SAED patterns of as-prepared $CaW_{1-x}Mo_xO_4$:Eu^{3+} ("x" = 0, 0.2, 0.4, 0.6, 0.8, and 1) nanowires are highlighted as insets to parts D−F and J−L, respectively.

single crystalline nature, as "x" increased, as shown in HRTEM images (Figure 4D−F and 4J−L), respectively. Ultimately, the presence of visible, distinctive two-dimensional (2D) lattice fringes at "x" = 0.8 and 1 clearly imply that the 1D $CaW_{1-x}Mo_xO_4$:Eu^{3+} nanowires at "x" = 0.8 and 1 are single crystalline with little if any apparent defects or dislocations (Figure 4K and L). Moreover, on the basis of the SAED patterns (insets to Figure 4D−F and 4J−L), the presence of sharp diffraction spots, as opposed to ring patterns associated with residual structure polycrystallinity, is more clearly distinctive as "x" increases.

Indeed, the SAED patterns consist of perfectly ordered and sharp diffraction spots at "x" = 0.8 and 1 (inset to Figure 4K

and L, respectively), thereby confirming the likely formation of single-crystalline $CaW_{1-x}Mo_xO_4$:Eu^{3+} nanowires at "x" = 0.8 and 1, under our modified template-directed methodology under room temperature, ambient conditions. The transition and apparent transformation from a polycrystalline to a single crystalline material as "x" increases are suggestive of an Ostwald ripening process in which larger crystallites grow at the expense of smaller constituent crystallites which in turn selectively dissolve away.[49,50] This hypothesis is consistent with the observation of larger crystallite sizes at larger "x", as estimated by the Debye−Scherrer formula in Figure 1 and described in section 3.1.
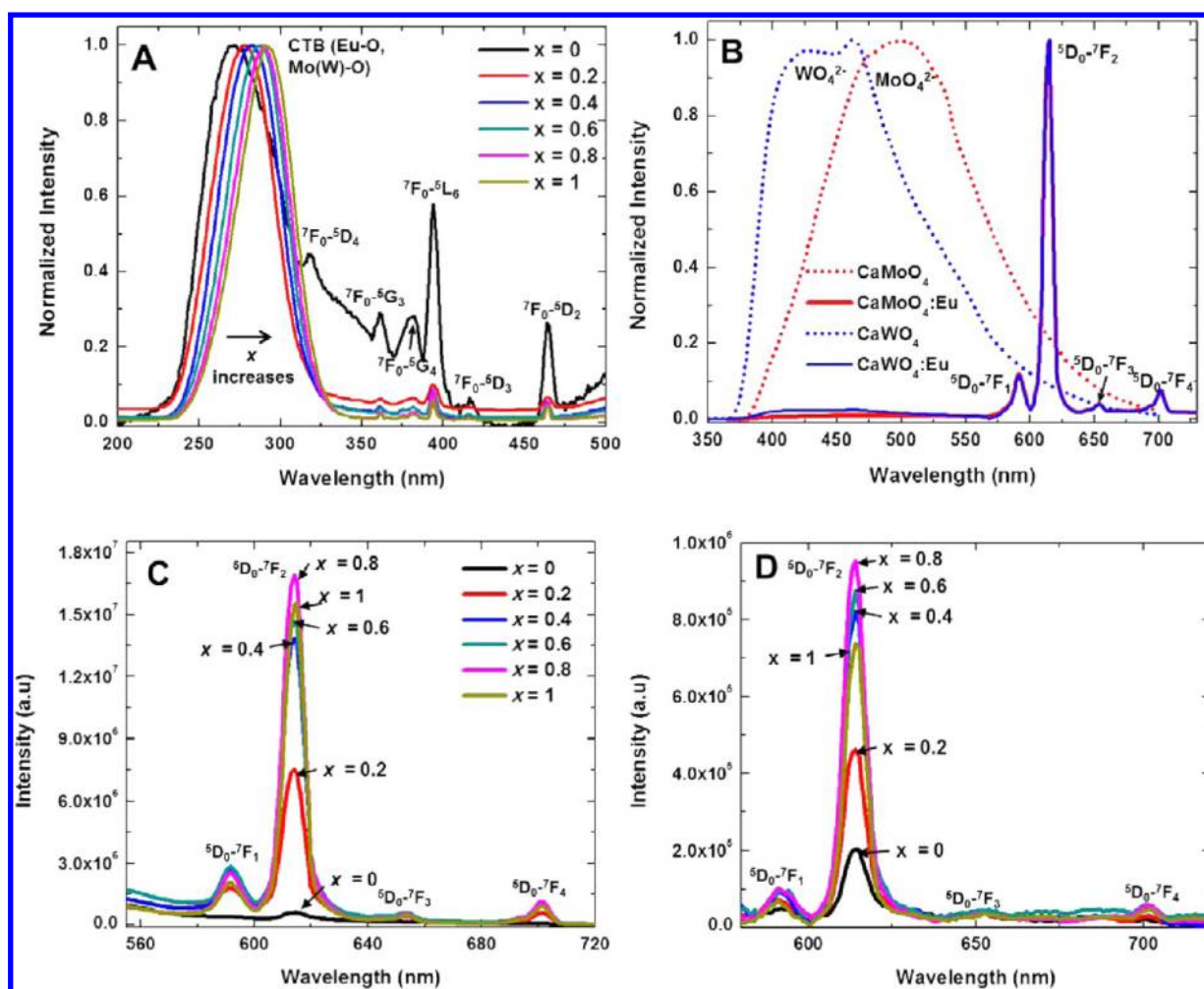
Figure 5. (A) PL excitation spectra of nanowires of as-prepared 1D $CaW_{1-x}Mo_xO_4:Eu^{3+}$ ("x" = 0, 0.2, 0.4, 0.6, 0.8, and 1). PL emission spectra of (B) undoped $CaMoO_4$ and $CaWO_4$ as well as of Eu^{3+}-activated $CaMoO_4$ and $CaWO_4$ under 280 nm excitation and of nanowires of $CaW_{1-x}Mo_xO_4:Eu^{3+}$ ("x" = 0, 0.2, 0.4, 0.6, 0.8, and 1) under both (C) 280 nm and (D) 395 nm excitation conditions.

3.3. Luminescence Characteristics of 1D $CaW_{1-x}Mo_xO_4:Eu^{3+}$ Nanostructures.

Figure 5 highlights the PL excitation and emission spectra of $CaW_{1-x}Mo_xO_4:Eu^{3+}$ under UV (280 nm) and near UV (395 nm) excitation, respectively. PL excitation spectra exhibit a broad, metal-oxide-specific excitation band near 270−290 nm, which can be ascribed to the O^{2-}−Eu^{3+} charge transfer band. The weaker peaks in the longer wavelength region can be assigned to f–f transitions of Eu^{3+} from its ground state ($^7F_0$) to possible excited states (i.e., $^5L_6$, $^5D_{2,3,4}$, and $^5G_{3,4}$) within the Eu^{3+} $4f$ configuration, monitored at 614 nm emission. The broad band excitation spectra near 270−290 nm are attributable to the presence of charge transfer between the oxygen and either the tungsten or molybdenum atoms within the anion complex of WO_4^{2-} or MoO_4^{2-}. In particular, it is well known that upon excitation from O_{2p} to either the W_{t2g} or Mo_{t2g} states, the WO_4^{2-} or MoO_4^{2-} groups effectively absorb ultraviolet irradiation within the $CaWO_4$ or $CaMoO_4$ construct, respectively.[14,51,52] We note that the main peak position of the excitation band of $CaMoO_4$ (located at ∼292 nm) is obviously red-shifted as compared with that of $CaWO_4$ (270 nm), as shown in Figure 5A. More importantly, all samples display a single broad band near 270−290 nm, and the peak position is gradually more red-shifted as "x" increases within the series of $CaW_{1-x}Mo_xO_4:Eu^{3+}$, thereby further confirming the

formation of a homogeneous, uniform, and "ideal" solid-solution of our 1D $CaW_{1-x}Mo_xO_4:Eu^{3+}$ with little if any impurities. We do not appear to find evidence for the presence of unreacted compounds of either $CaWO_4$ or $CaMoO_4$ in our series.

Furthermore, we observed excitation features in the region of 318, 361, 381, 395, 418, and 464 nm, consistent with transitions associated with $^7F_0$–$^5D_4$, $^7F_0$–$^5G_3$, $^7F_0$–$^5G_4$, $^7F_0$–$^5L_6$, $^7F_0$–$^5D_3$, and $^7F_0$–$^5D_2$ of Eu^{3+}, respectively. We note that these peak positions are independent of "x" in $CaW_{1-x}Mo_xO_4:Eu^{3+}$, since the f–f transitions of Eu^{3+} are not strongly affected by the underlying metal oxide host lattice itself.[10] Nonetheless, the presence of the broad excitation band related to the host lattice (mainly the WO_4^{2-} and MoO_4^{2-} groups), when monitored at 614 nm, can be assigned to the characteristic emission of Eu^{3+} ($^5D_0$−$^7F_2$), thereby indicating that there is likely to be energy transfer from either the WO_4^{2-} or MoO_4^{2-} groups to the Eu^{3+} activator ions within our 1D $CaW_{1-x}Mo_xO_4:Eu^{3+}$ nanowires.

Additional evidence for energy transfer from either the WO_4^{2-} or MoO_4^{2-} groups to the Eu^{3+} activator ions is provided by the PL emission spectra of undoped $CaWO_4$ and $CaMoO_4$ and of the corresponding Eu^{3+}-activated $CaWO_4$ and $CaMoO_4$ under 260 nm excitation (Figure 5B). We find that the PL emission spectrum is normalized by the highest PL emission intensity of 1. The PL spectra of undoped $CaWO_4$ and

$CaMoO_4$ exhibit a broad emission peak near 420 and 500 nm, respectively. The characteristic broad emission band near 420 nm for $CaWO_4$ and near 500 nm for $CaMoO_4$ can be potentially assigned to the intrinsic emission of the $CaWO_4$ and $CaMoO_4$ structure. Specifically, in this excited state, the holes (on the oxygen O_{2p}) and the electrons (on either the tungsten (W_{t2g}) or the molybdenum (Mo_{t2g}) within either the WO_4^{2-} or MoO_4^{2-} groups) are more likely to interact, combine, and effectively form an exciton, with the generation of a strong emission band near 420−500 nm.[14,51,52]

The emission peak position of $CaMoO_4$ is red-shifted as compared with that of $CaWO_4$, an observation consistent with the excitation spectra shown in Figure 5A as well as with other reports,[14] which assigned this particular observation to a smaller crystal field splitting of MoO_4^{2-} as compared with that of WO_4^{2-}. When Eu^{3+} activators are incorporated into these materials, the broad band emission from either the WO_4^{2-} or MoO_4^{2-} groups is dramatically quenched, while simultaneously, a distinctive and strong sharp emission appears, corresponding to the transition between the excited states of $^5D_0$ and the ground states of ^7F_J (J = 1, 2, 3, and 4) of Eu^{3+}. The PL quenching of either the WO_4^{2-} or MoO_4^{2-} groups coupled with the appearance of strong $^5D_0-^7F_J$ (J = 1, 2, 3, and 4) transitions associated with Eu^{3+} provides for direct evidence of an efficient energy transfer from either the WO_4^{2-} or MoO_4^{2-} groups to the Eu^{3+} activator ions.

The PL emission spectra of $CaW_{1-x}Mo_xO_4$:Eu^{3+} nanowires ("x" = 0, 0.2, 0.4, 0.6, 0.8, and 1) excited at 280 and 395 nm are shown in Figure 5C and D, respectively. These excitation wavelengths were chosen, since we can examine the composition-dependent PL emission characteristics of our solid-solution composites more efficiently under both host lattice-directed (280 nm) and rare earth activator-specific (395 nm) excitation conditions. We found that the PL emission spectra of all samples clearly exhibit the characteristic line features, associated with Eu^{3+} emission at 592, 614, 654, and 702 nm, which can be correlated with the $^5D_0-^7F_1$, $^5D_0-^7F_1$, $^5D_0-^7F_1$, and $^5D_0-^7F_1$ transitions of Eu^{3+}, respectively, under both 280 and 395 nm excitation. These data imply that our solid-solution nanowires are likely well crystallized and that the observed emission originating from defect sites (such as the presence of vacancies arising from the charge imbalance between Ca^{2+} and Eu^{3+}) is negligible. Interestingly, our results also suggest that the emission intensity of our 1D $CaW_{1-x}Mo_xO_4$:Eu^{3+} increases with and correlates with "x", with the highest intensity observed when "x" = 0.8, again under excitation conditions of both 280 and 395 nm (Figures 5C,D and 6).

In Figure 6, the PL emission intensity as a function of "x" can be functionally explained in light of two factors, namely (a) the intrinsic crystallite size and inherent crystallinity as well as (b) the presence of efficient $Eu^{3+}-Eu^{3+}$ interactions. *First*, (a) the PL intensity and associated PL quantum efficiency (PL QE) are strongly affected by the structural characteristics of the host lattice itself (i.e., crystallite size, purity, and the presence of single crystallinity), since either surface or intercalation defect sites within the host lattice can provide for a number of possible nonradiative recombination routes for electrons and holes, which would thereby lead to quenching of the luminescence output.[53,54] In our 1D $CaW_{1-x}Mo_xO_4$:Eu^{3+} solid-solution composites, as discussed earlier, we have observed that both the crystallite size and degree of single crystallinity actually increase with increasing Mo content (i.e., as a function of
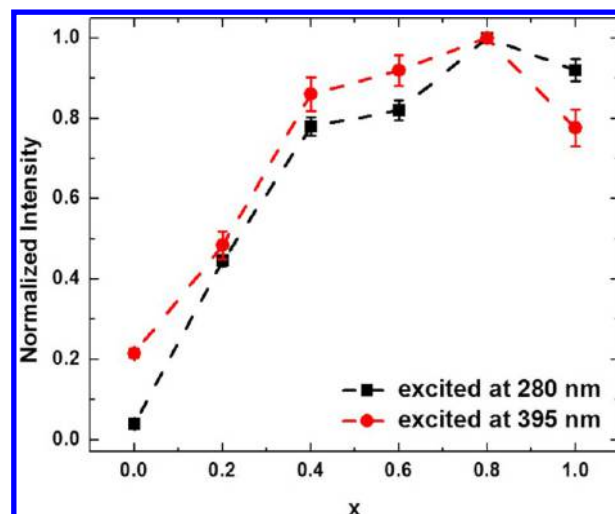

Figure 6. Normalized PL emission intensity of the Eu^{3+} emission in $CaW_{1-x}Mo_xO_4$:Eu^{3+} as a function of increasing "x" under both 280 and 395 nm excitation conditions. We normalized the PL intensity collected on $CaW_{1-x}Mo_xO_4$:Eu^{3+}, when "x" = 0.8, to be 1.

increasing "x"). Not surprisingly, the sample with a relatively larger crystallite size and with a high degree of single crystallinity, e.g. with "x" = 0.8, on the basis of the diffraction and microscopy data, yielded the highest PL intensity observed. By contrast, as expected, samples possessing a smaller crystallite size and a lower degree of crystallinity, e.g., with "x" = 0.4, gave rise to decreased PL intensities.

Second, (b) the $Eu^{3+}-Eu^{3+}$ distance within a molybdate environment (average distance: 3.86(6) Å) is actually shorter than that in the corresponding tungstate matrix (average distance: 3.9(1) Å).[55−57] This fact implies that stronger ion pair interactions occur between Eu^{3+} ions within molybdates as compared with within tungstates, which can lead to more efficient energy transfer between the two ions and which is consistent with other reports of analogous systems. For example, Chiu et al.[58] reported on a $LiEu(WO_4)_{2-x}(MoO_4)_x$ solid-solution and found that the intensity of the $^5D_0-^7F_2$ emission of the dopant Eu^{3+} activator noted at wavelengths of 396 nm correlated with increasing ratios of Mo/W. Zeng et al.[59] discerned a similar trend with respect to the PL intensity of Eu^{3+} as a function of Mo composition, and showed that the highest emission of Eu^{3+} could be observed within $BaGd_2(W_{1-x}Mo_xO_4)_4$ with "x" = 0.9. Similar increases in the PL emission intensity of dopant metal ions have also been detected in complex bulk systems including $NaM(WO_4)_{2-x}(MoO_4)_x$ (M = Gd^{3+}, Y^{3+}, and Bi^{3+}),[60] $M_5Eu(WO_4)_{4-x}(MoO_4)_x$ (M = Li^+, Na^+, and K^+),[61] and $AgGd_{0.95}Eu_{0.05}(WO_4)_{2-x}(MoO_4)_x$[62] respectively.

3.4. Structural Insights into $CaW_{0.2}Mo_{0.8}O_4$:Eu^{3+}−CdSe and CdS QD Heterostructures.

Figures 7A and B highlight typical TEM images collected on as-prepared composites of 1D $CaW_{0.2}Mo_{0.8}O_4$:Eu^{3+} nanowire−(0D CdSe QD or CdS QD) heterostructures, respectively, chosen because of their expected favorable optical attributes. Complications associated with the lack of a sizable contrast variation between the CdSe/CdS QDs and the $CaW_{0.2}Mo_{0.8}O_4$:Eu^{3+} nanowires prevented a clear and marked differentiation between the two different nanostructures, especially in the inner surface region of the $CaW_{0.2}Mo_{0.8}O_4$:Eu^{3+} nanowires. Nonetheless, we have been able to discern distinctive spatial domains, wherein both CdSe

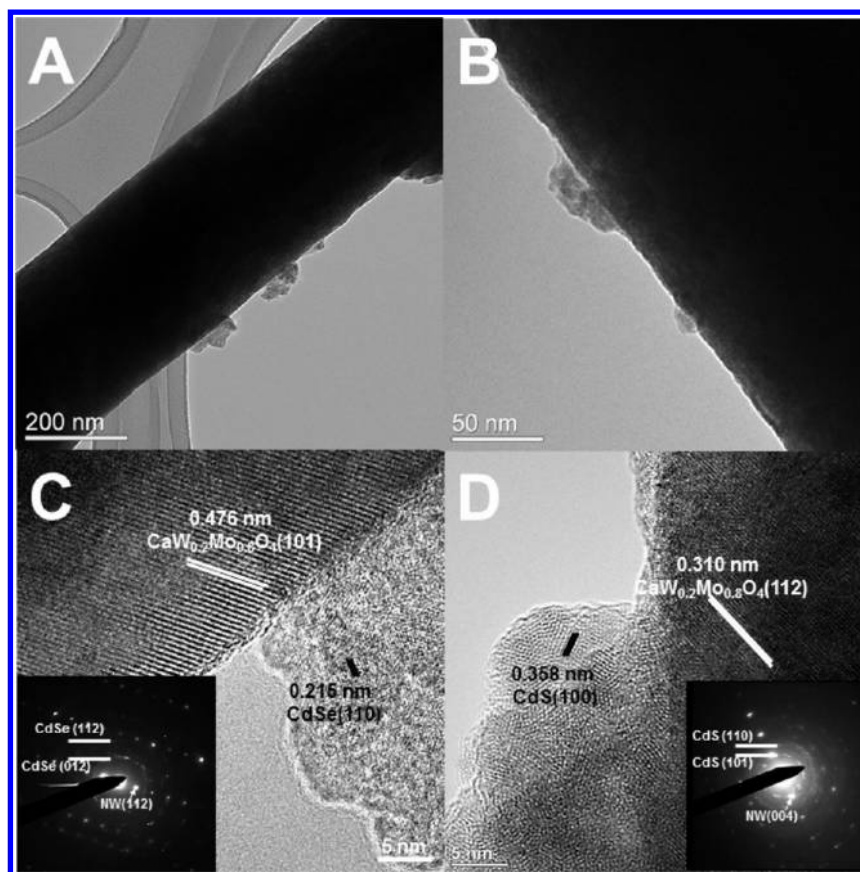**Figure 7.** Representative TEM and HRTEM images and the corresponding SAED patterns (insets to C and D), associated with the formation of $CaW_{0.2}Mo_{0.8}O_4{:}Eu^{3+}-$(0D CdSe (panels A and C) or CdS QD (panels B and D)) heterostructures, respectively. In parts C and D, NW denotes the corresponding $CaW_{0.2}Mo_{0.8}O_4{:}Eu^{3+}$ 1D nanowire reflections.
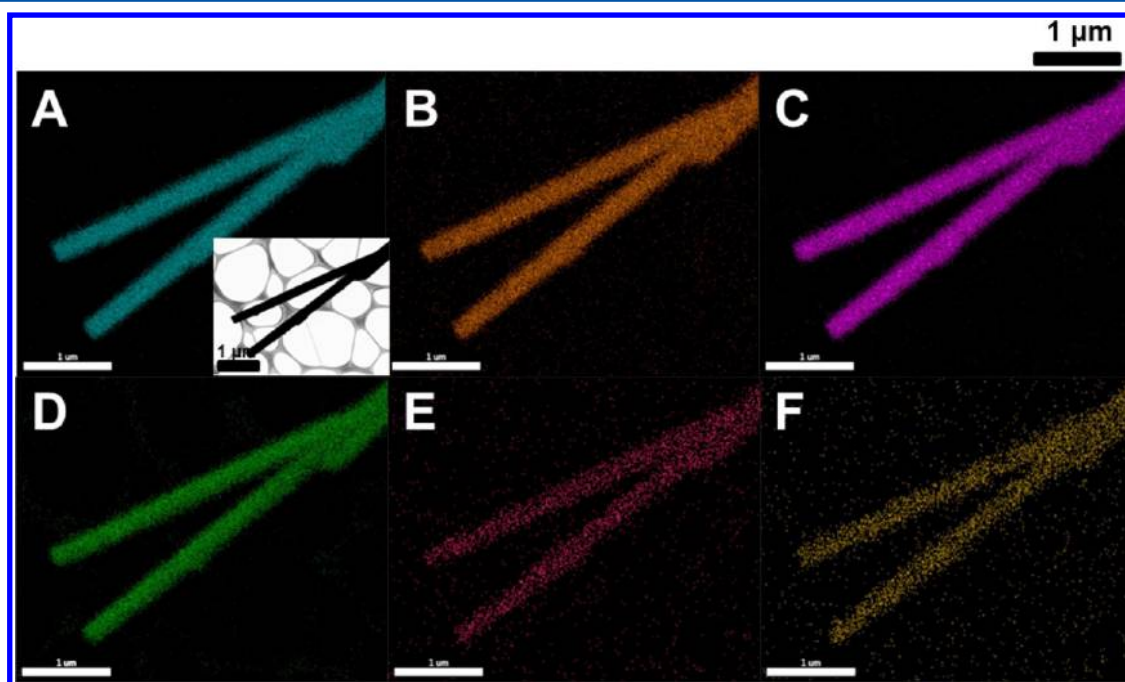

Figure 8. (A−F) Elemental EDS mapping data of the identical region of $CaW_{0.2}Mo_{0.8}O_4{:}Eu^{3+}-$CdSe QD heterostructures, highlighting the overlapping spatial chemical distribution of Ca (bright blue), W (orange), Mo (purple), O (green), Cd (bright red), and Se (green-yellow), respectively. Scale bar is 1 μm in every image. The corresponding dark-field STEM image is shown as an inset to part A.
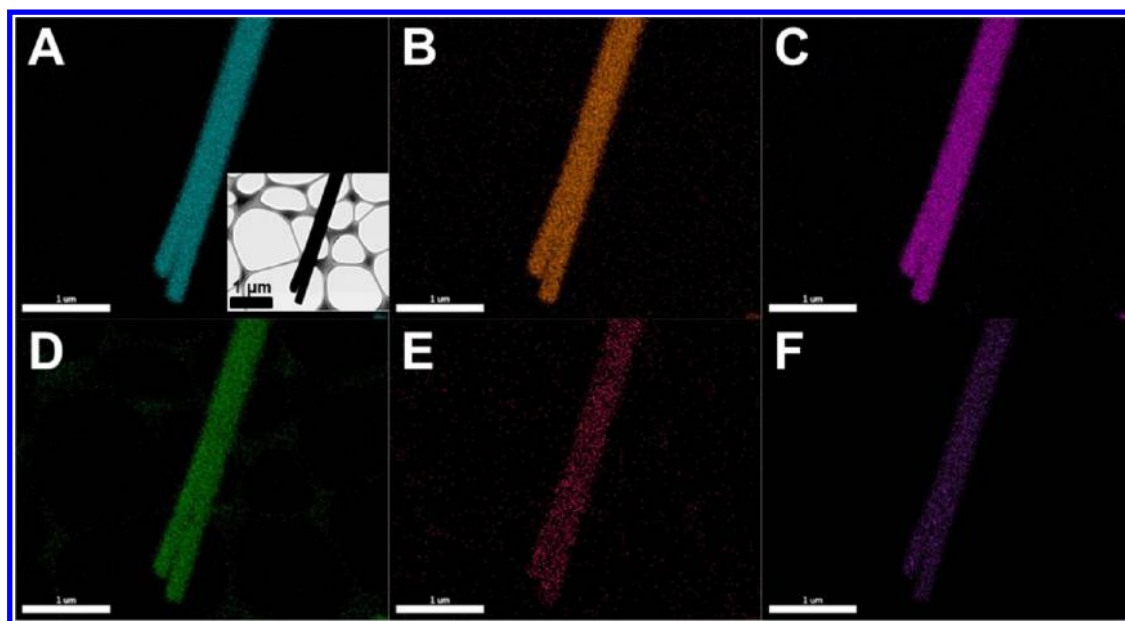
Figure 9. (A−F) Elemental EDS mapping of the identical region of $CaW_{0.2}Mo_{0.8}O_4$:Eu^{3+}−CdS QD heterostructures, highlighting the overlapping spatial chemical distribution of Ca (bright blue), W (orange), Mo (purple), O (green), Cd (bright red), and S (dark-purple), respectively. Scale bar is 1 μm in every image. The corresponding dark-field STEM image is shown as an inset to part A.

QDs (d ~2.7 nm) and CdS QDs (d ~3.5 nm) are clearly affixed and immobilized onto the underlying 1D $CaW_{0.2}Mo_{0.8}O_4$:Eu^{3+} nanowire structural motifs.

Specifically, the HRTEM images (Figure 7C and D) of an individual $CaW_{0.2}Mo_{0.8}O_4$:Eu^{3+} nanowire−QD heterostructure incorporating CdSe and CdS QDs, respectively, unequivocally indicate that highly crystalline CdSe QDs and CdS QDs can be closely bound onto the underlying 1D $CaW_{0.2}Mo_{0.8}O_4$:Eu^{3+} nanowire motifs. In addition, HRTEM revealed an interlayer spacing of 0.215 and 0.476 nm, respectively, in good agreement with the expected d spacings of the (110) and (101) lattice planes, respectively, corresponding to the hexagonal structure of CdSe QDs and scheelite 1D $CaW_{0.2}Mo_{0.8}O_4$:Eu^{3+} nanowires (Figure 7C), respectively. By analogy, for the other heterostructures, the 0.358 and 0.310 nm measured for the (100) and (112) planes were consistent with expected data for the würtzite structure of CdS QDs and 1D $CaW_{0.2}Mo_{0.8}O_4$:Eu^{3+} nanowires, respectively. The associated SAED patterns (i.e., insets to Figure 7C and D) of the heterostructures mainly consist of sharp diffraction spots, due to the single crystallinity of the $CaW_{0.2}Mo_{0.8}O_4$:Eu^{3+} nanowires and the inherent crystallinity of the CdSe QDs and CdS QDs, as well. Particular features associated with the individual discrete diffraction patterns nevertheless could be specifically and reliably assigned either to $CaW_{0.2}Mo_{0.8}O_4$:Eu^{3+} nanowires or to CdSe and CdS QDs, as indicated by the insets to Figure 7C and D, respectively.

In order to more precisely examine the spatial distribution of the elemental composition throughout our heterostructures, so as to confirm the presence of QDs within our composites and to thereby deduce the corresponding QD coverage, a detailed chemical analysis was carried out using energy-dispersive X-ray spectroscopy (EDS). Specifically, elemental maps of heterostructures composed of $CaW_{0.2}Mo_{0.8}O_4$:Eu^{3+} nanowire−CdSe QD and of $CaW_{0.2}Mo_{0.8}O_4$:Eu^{3+} nanowire−CdS QD composites are, respectively, highlighted in Figures 8A−F and 9A−F. These data provide insight into the spatial localization of the various constituent elements and components associated with

both QD and metal oxide nanowire species, i.e., Ca, W, O, Mo, Cd, Se, and S. The STEM images, designating the elemental maps for heterostructures composed of $CaW_{0.2}Mo_{0.8}O_4$:Eu^{3+} nanowire−CdSe QD and of $CaW_{0.2}Mo_{0.8}O_4$:Eu^{3+} nanowire−CdS QD composites, have been provided as insets to Figures 8A and 9A, respectively.

In panels E and F of Figures 8 and 9, the locations of the Cd L-edge, the Se K-edge, and the S K-edge signals overlap and coincide reasonably well with those of the Ca K-edge, the W L-edge, the Mo K-edge, and the O K-edge signals (Figures 8 and 9A−D), thereby suggesting that CdSe and CdS QDs are uniformly "sprinkled" onto and evenly distributed throughout the outer external surfaces of 1D $CaW_{0.2}Mo_{0.8}O_4$:Eu^{3+}−(0D CdSe QD or CdS QD) heterostructures. In order to further confirm and corroborate the qualitative coverage density as estimated by EDS mapping data (i.e., Figures 8 and 9, and Supporting Information Figure S3), we performed a more rigorous quantitative analysis in order to ascertain the actual coverage density of both CdSe QDs and CdS QDs on the underlying $CaW_{0.2}Mo_{0.8}O_4$:Eu^{3+} structures.

Our results show that approximately 3.2−3.4 QDs were attached onto 1D $CaWO_4$ nanowires upon normalization to identical surface areas (i.e., 10 nm^2) of underlying 1D nanowires and that these values were irrespective of the identity of the QDs, i.e., whether it was either CdS or CdSe QDs. These data are not surprising, since the "reagent" concentrations of both CdSe QDs and CdS QDs relative to that of the underlying 1D $CaW_{0.2}Mo_{0.8}O_4$:Eu^{3+} used in the generation of these heterostructures were identical, as previously mentioned in the Experimental Section. We describe our detailed reasoning and the mathematical protocol used to obtain these coverage values much more extensively in the associated Supporting Information.

3.5. Optical Data on $CaW_{0.2}Mo_{0.8}O_4$:Eu^{3+} Nanowire−CdSe/CdS QD Heterostructures. Figure 10 provides UV−vis extinction spectra of 1D Eu^{3+}-activated $CaW_{0.2}Mo_{0.8}O_4$ nanowires and MPA capped-CdSe and CdS QDs as well as of the resulting heterostructures, respectively. Control samples

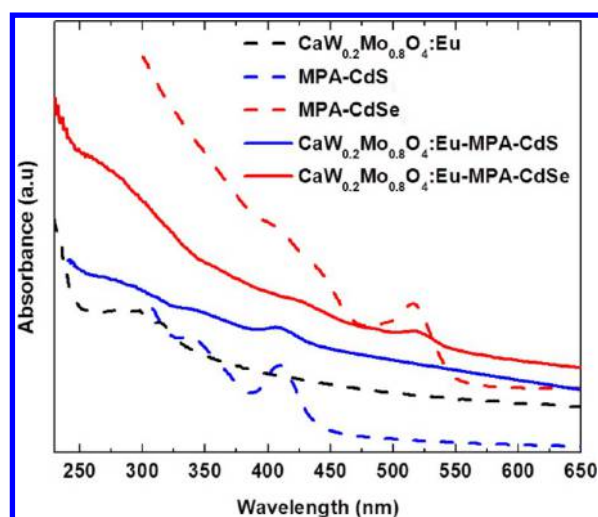**Figure 10.** UV−vis spectra of MPA-capped CdSe QDs and CdS QDs, $CaW_{0.2}Mo_{0.8}O_4:Eu^{3+}$ nanowires, and the resulting composite heterostructures, incorporating these constituent starting materials, respectively.

consisting of unbound MPA-capped CdSe and CdS QDs exhibit pronounced absorption peaks at ∼514 and ∼410 nm, respectively. Furthermore, $CaW_{0.2}Mo_{0.8}O_4:Eu^{3+}$ nanowires give rise to distinctive absorption peaks near 280−300 nm, which are consistent with the excitation spectra, shown in Figure 5A. Indeed, the UV−vis extinction spectra of both CdSe and CdS QD-based heterostructures suggest and reflect the presence of QDs immobilized onto the external surfaces of 1D $CaW_{0.2}Mo_{0.8}O_4:Eu^{3+}$ nanowires.

Steady-state PL emission spectra of MPA-capped CdSe QDs, $CaW_{0.2}Mo_{0.8}O_4:Eu^{3+}$ nanowires, $CaW_{0.2}Mo_{0.8}O_4:Eu^{3+}$ nanowire−CdSe QD heterostructures, as well as $CaW_{0.2}Mo_{0.8}O_4:Eu^{3+}$ nanowire−CdS QD heterostructures, all of which were collected at 300 nm excitation, are highlighted in Figure 11A. Specifically, the emission spectra of "free" CdSe QDs consist of a high-energy peak, corresponding to a strong band edge emission located at 521 nm, accompanied by a weak but non-negligible surface trap emission in the near-infrared region, originating from the presence of photoexcited hole trapping ligands (i.e., MPA) on the external surface of these quantum confined nanomaterials. The characteristic sharp
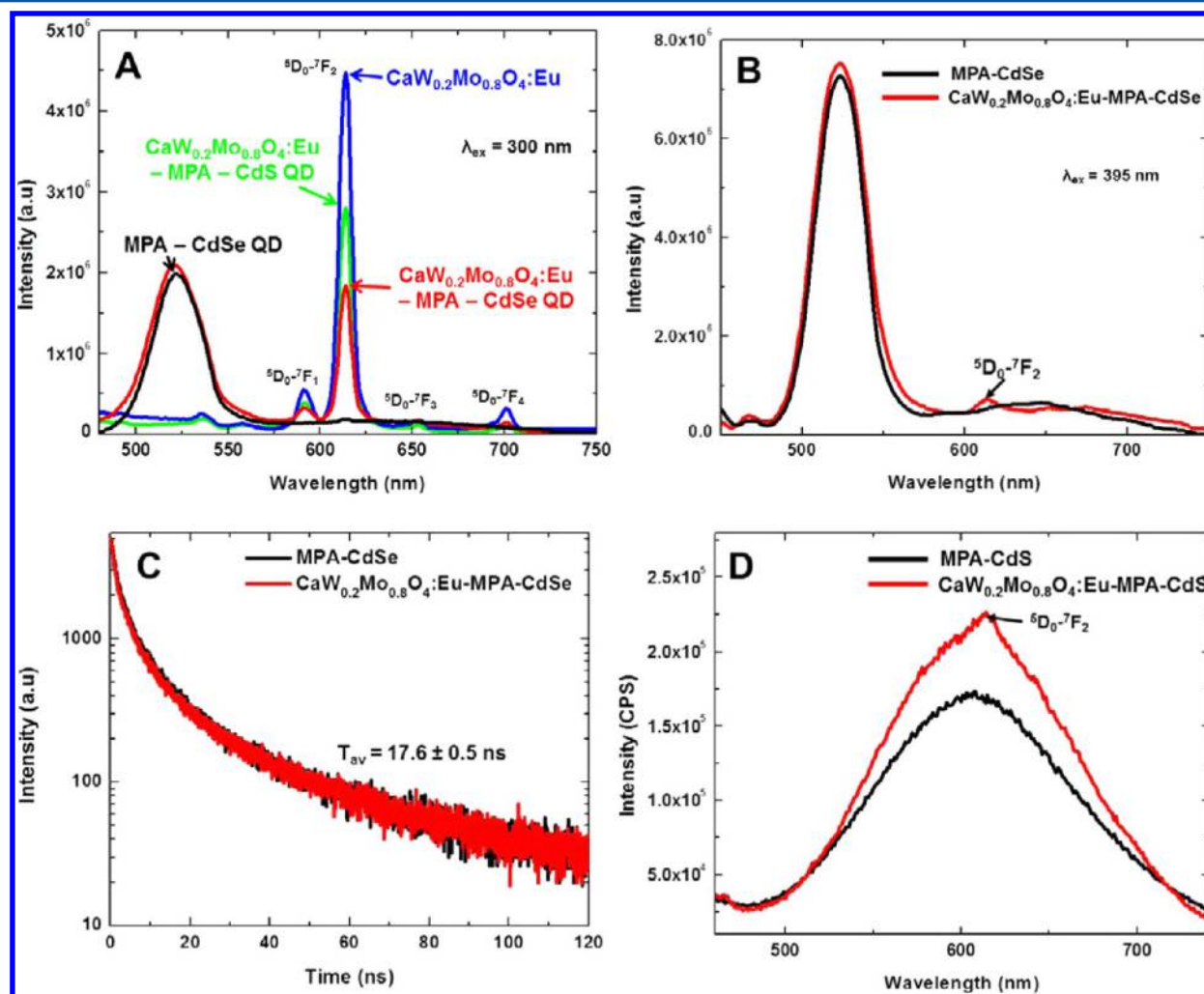

Figure 11. PL emission spectra of (A) $CaW_{0.2}Mo_{0.8}O_4:Eu^{3+}$−CdS QD heterostructures, $CaW_{0.2}Mo_{0.8}O_4:Eu^{3+}$−CdSe QD heterostructures, $CaW_{0.2}Mo_{0.8}O_4:Eu^{3+}$ nanowires, and MPA-capped CdSe QDs, excited at 300 nm. (B) PL emission spectra of $CaW_{0.2}Mo_{0.8}O_4:Eu^{3+}$−CdSe QD heterostructures and of MPA-capped CdSe QDs under 395 nm excitation. (C) PL decay curves ($\lambda_{ex} = 388$ nm) associated with the excitonic emission of MPA-capped CdSe QDs and of $CaW_{0.2}Mo_{0.8}O_4:Eu^{3+}$ nanowire−CdSe QD heterostructures. (D) PL emission spectra of $CaW_{0.2}Mo_{0.8}O_4:Eu^{3+}$ nanowire−CdS QD heterostructures and of MPA-capped CdS QDs under 395 nm excitation.

emission observed in the region from 575−720 nm can be assigned to the $^5D_0−^7F_J$ (with J = 1, 2, 3, and 4) transitions of Eu^{3+} incorporated within $CaW_{0.2}Mo_{0.8}O_4:Eu^{3+}$ nanowires, as has been discussed in section 3.3.

Interestingly, the emission intensity of $CaW_{0.2}Mo_{0.8}O_4:Eu^{3+}$ within both heterostructures composed of $CaW_{0.2}Mo_{0.8}O_4:Eu^{3+}$ nanowires coupled with either CdSe QDs or CdS QDs is substantially reduced as compared with unbound $CaW_{0.2}Mo_{0.8}O_4:Eu^{3+}$ subunits. Furthermore, the extent of the PL quenching of $CaW_{0.2}Mo_{0.8}O_4:Eu^{3+}$ within the CdSe QD-based heterostructure is more pronounced as compared with that in the CdS QD-based heterostructure. Specifically, the emission intensity of $CaW_{0.2}Mo_{0.8}O_4:Eu^{3+}$ incorporated in CdSe QD-based heterostructures and CdS QD-based heterostructures quenches by a factor of 2.4 and 1.6, respectively, by comparison with "free" $CaW_{0.2}Mo_{0.8}O_4:Eu^{3+}$. We propose that the PL quenching of $CaW_{0.2}Mo_{0.8}O_4:Eu^{3+}$ observed within these heterostructure motifs can be mainly attributed to photoexcited charge (i.e., electron) transfer from $CaW_{0.2}Mo_{0.8}O_4:Eu^{3+}$ to both CdSe QDs and CdS QDs. This assertion makes sense in light of the inherent band alignments of the various species involved. Specifically, the energy levels of the conduction band edges (CBs) of both $CaMoO_4$ and $CaWO_4$ are situated above those of CdSe QDs and CdS QDs (Figure 12), respectively, thereby resulting in potentially favorable photoinduced electron flow into the CdSe QDs and CdS QDs from the metal tungstate−molybdate solid-solution composite.
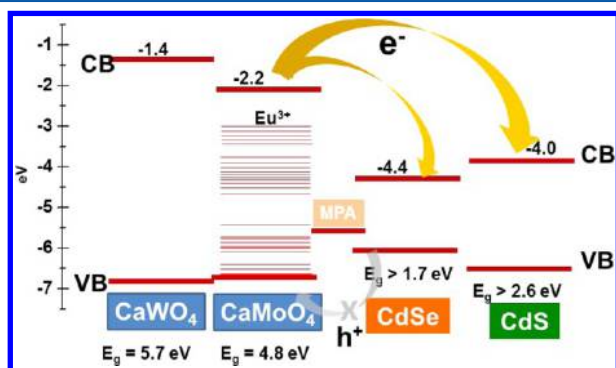

Figure 12. Electronic energy diagram describing plausible electronic interactions in $CaWO_4−CaMoO_4:Eu^{3+}$−MPA-capped CdS QD heterostructures and the corresponding $CaWO_4−CaMoO_4:Eu^{3+}$−MPA-capped CdSe QD heterostructures. Corresponding possible charge transfer pathways in these materials are shown: e^- = electron, h^+ = hole, E_g = band gap, CB = conduction band, and VB = valence band.

In order to examine the analogous luminescent properties of CdSe QDs and CdS QDs within the 1D−0D heterostructure, we collected PL spectra of 1D $CaW_{0.2}Mo_{0.8}O_4:Eu^{3+}$ nanowire−(0D CdSe QD or CdS QD) heterostructures, excited under 395 nm illumination conditions (Figure 11B and C, respectively). We should note that the intrinsic PL signature of $CaW_{0.2}Mo_{0.8}O_4$ within our heterostructures under 395 nm excitation can be potentially overwhelmed by the emission of either MPA-capped CdSe QDs or CdS QDs. The small "hilly" feature located near 614 nm may be ascribed to the $^5D_0−^7F_2$ transition of Eu^{3+}.

The optical profiles of the QDs themselves do not appear to perceptibly alter upon their immobilization onto the underlying metal oxide nanowires. That is, by contrast with the very

noticeable and dramatic PL quenching behavior of $CaW_{0.2}Mo_{0.8}O_4:Eu^{3+}$ within our heterostructures under 300 nm excitation, the corresponding variation of PL intensity near the QD band gap (i.e., ~523 nm) as well as any possible fluctuations in the trap emission located near the IR region of MPA-capped CdSe QDs within the heterostructures seem relatively muted and less significant, even under both 300 and 395 nm excitation conditions (Figure 11A and B, respectively). These collective data strongly suggest that not only the charges localized on the CdSe QDs but also the trapped charges within MPA-capped CdSe QDs are not being transferred to any appreciable degree onto adjoining $CaW_{0.2}Mo_{0.8}O_4:Eu^{3+}$ nanowires.

This hypothesis is further confirmed by the emission decay behavior observed near the band gap emission (i.e., ~523 nm), as shown in Figure 11C. The PL decay curves of unbound MPA-capped CdSe QDs are not substantially different from the corresponding profiles of CdSe QDs bound onto and attached onto $CaW_{0.2}Mo_{0.8}O_4:Eu^{3+}$ nanowires. In fact, the average lifetimes of free, unbound MPA-capped CdSe QDs and of CdSe QDs immobilized within our heterostructures are comparable (τ_{av} = 17.6 ± 0.3 ns). Similarly, there is no substantial evidence to support the idea of charge transfer occurring from MPA-capped CdS QDs to $CaW_{0.2}Mo_{0.8}O_4:Eu^{3+}$ nanowires in $CaW_{0.2}Mo_{0.8}O_4:Eu^{3+}$ nanowire−CdS QD heterostructures.

We observed a broad band emission in the range of 460−720 nm under 395 nm excitation (Figure 11D), which may originate from the trap state emission of CdS QDs due to the presence of MPA ligands. If true, we note that this putative trap emission band becomes even more enhanced within the heterostructure, an observation which may derive from the generation of additional trap sites and defects, associated with the formation of the heterostructure itself.[63,64]

We should also mention that the band gap emission of MPA-capped CdS QDs is close to the detection limit of our PL instrument, whereas the emission of MPA-capped CdSe QDs is comparatively stronger and more apparent (Supporting Information Figure S4 and Figure 11A). Nonetheless, the signal for MPA-capped CdS QDs is presumably located in the region of 425−435 nm, where as-prepared CdS QDs capped with myristic acid (i.e., CdS QDs before the ligand exchange with MPA) display a strong and broad signal feature near 428 nm (Supporting Information Figure S4). The key lesson learned is that MPA can potentially be a more effective PL quencher (i.e., a photoexcited hole acceptor) for CdS QDs as compared with CdSe QDs, when the native ligands on the QD surface are replaced with MPA. This does make logical sense, since the energy band offset between CdS and MPA is noticeably larger than that between CdSe and MPA (Figure 12).

3.6. Data Interpretation in Terms of Energy Level Alignments. Figure 12 depicts a schematic diagram, detailing the energy levels associated with all of the various disparate constituent species in our system, i.e., $CaWO_4$, $CaMoO_4$, CdSe QDs, and CdS QDs, respectively. These data have come from different sources. For instance, Longo et al.[65] and Zhang et al.[14] have, respectively, reported on the electronic levels of $CaWO_4$ and $CaMoO_4$, derived using both experimental techniques (TEM and HRTEM) as well as *ab initio* and theoretical DFT calculations. Furthermore, Cavalli et al.[66] and Dorenbos et al.[67] have provided insight into the electronic level structure of rare-earth-activated $CaWO_4$ and $CaMoO_4$. On the basis of these

cumulative prior efforts, it is reasonable to assert that the conduction band (CB) of $CaW_{0.2}Mo_{0.8}O_4{:}Eu^{3+}$ is situated between that of $CaWO_4$ (i.e., -1.4 eV relative to the vacuum level) and $CaMoO_4$ (i.e., $\sim$-2.2 eV), but it is located above the corresponding CB of CdSe QDs (i.e., -4.4 eV)[37] as well as that of CdS QDs (i.e., -4.0 eV).[68] According to Marcus theory,[69] the driving force for charge transfer is affected by the CB potentials of both charge donor and acceptor materials.

In this light, the evident band offset between $CaW_{0.2}Mo_{0.8}O_4{:}Eu^{3+}$ and either CdS QDs or CdSe QDs can lead to an expected PL quenching as a result of electron transfer occurring from $CaW_{0.2}Mo_{0.8}O_4{:}Eu^{3+}$ to either CdS or CdS QDs, when the $CaW_{0.2}Mo_{0.8}O_4{:}Eu^{3+}$ 1D subunits are specifically optically excited, as shown in Figure 10A. Similarly, the PL quenching behavior of $CaW_{0.2}Mo_{0.8}O_4{:}Eu^{3+}$ within the CdSe QD-based heterostructures is predictably more pronounced as compared with that observed within the CdS QD-based heterostructures, because there is a larger CB band offset between $CaW_{0.2}Mo_{0.8}O_4{:}Eu^{3+}$ and CdSe QDs ($\sim$2.2 eV) as compared with that between $CaW_{0.2}Mo_{0.8}O_4{:}Eu^{3+}$ and CdS QDs ($\sim$1.4 eV).

Conversely, photoexcited holes generated in the CdSe and CdS QDs can be very efficiently trapped within the MPA linker, due to the higher redox potential of the ligand (e.g., VB ~ -5.5 eV)[70] as compared with that of both CdSe QDs (e.g., VB ~ -6.1 eV)[37] and CdS QDs (e.g., VB ~ -6.6 eV).[68] Furthermore, both the photoinduced holes trapped within MPA and the holes and electrons confined in QDs are not likely to migrate into $CaW_{0.2}Mo_{0.8}O_4{:}Eu^{3+}$, due to the unfavorable band alignment present, thereby explaining the minimal reduction of the PL output associated with both CdSe and CdS QDs incorporated within these heterostructures.

3.7. Confirmation with NEXAFS Measurements. In order to further confirm (i) the presence of electron transfer from our 1D Eu^{3+}-activated $CaWO_4$–$CaMoO_4$ solid-solution onto adjacent MPA-capped CdSe QDs as well as CdS QDs and to account for (ii) the observed PL quenching of $CaW_{0.2}Mo_{0.8}O_4{:}Eu^{3+}$ within our as-prepared heterostructures, we collected relevant NEXAFS spectra. Specifically, we examined the spectra of the Cd $M_{2,3}$ edge, because the bottom of the CB in both CdSe and CdS QDs is predominantly defined by the Cd 5s state. Therefore, theory and calculations predict that studying alterations in the behavior of Cd $M_{2,3}$ edges should provide insight into the transition between the initial 3p state and the unoccupied 5s states.[71,72]

NEXAFS spectra associated with the Cd $M_{2,3}$ edge of 1D $CaW_{0.2}Mo_{0.8}O_4{:}Eu^{3+}$ nanowire–(0D CdSe QD or CdS QD) heterostructures as well as with both MPA-capped CdS QDs and CdSe QDs are shown in Figure 13A and B, respectively. Interestingly, when probing the Cd $M_{2,3}$ edge (at $\sim$618 eV), the normalized PEY intensity of the complex heterostructures composed of $CaW_{0.2}Mo_{0.8}O_4{:}Eu^{3+}$–CdSe QD and of $CaW_{0.2}Mo_{0.8}O_4{:}Eu^{3+}$–CdS QD was found to be noticeably reduced as compared with that of MPA-capped CdSe QDs and CdS QDs alone, respectively (Figure 13A,B). From prior studies, it is known that the PEY intensity is proportional to the unoccupied electronic density of states.[33,73,74] Hence, the decrease in the number of unoccupied states associated with the CB in MPA-capped CdSe QDs and CdS QDs incorporated as part of composite heterostructures versus that of the corresponding unbound and free MPA-capped CdSe QDs and CdS QDs is highly indicative of an increase in the number of electrons in the Cd 5s states (i.e., the CB of CdSe QDs), presumably emanating from $CaW_{0.2}Mo_{0.8}O_4{:}Eu^{3+}$ as a source of electrons
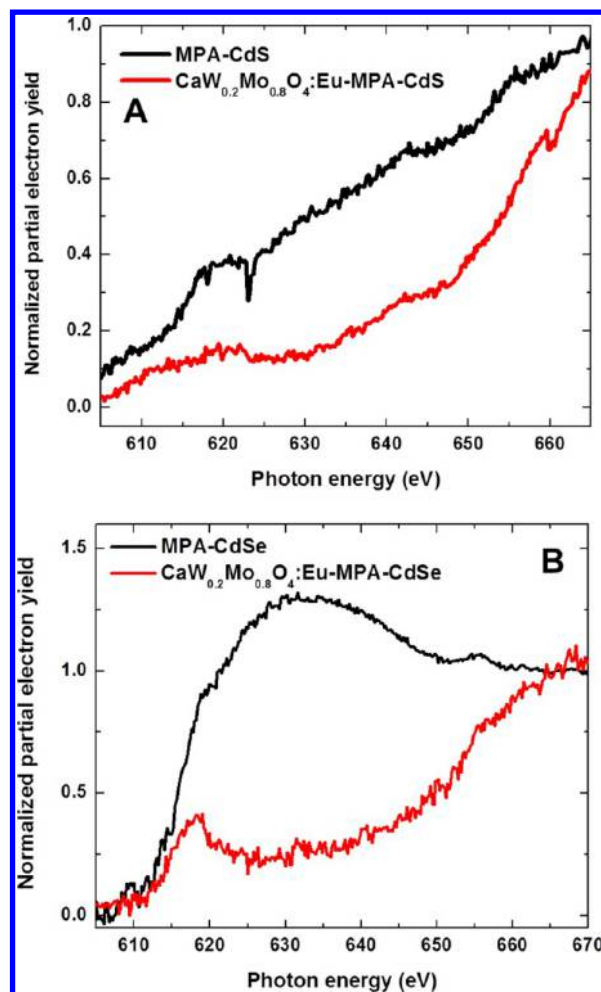

Figure 13. Cd $M_{2,3}$ edge partial electron yield spectra of (A) $CaW_{0.2}Mo_{0.8}O_4{:}Eu^{3+}$–CdSe QD heterostructures and MPA-capped CdSe QDs as well as of (B) $CaW_{0.2}Mo_{0.8}O_4{:}Eu^{3+}$–CdS QD heterostructures and MPA-capped CdS QDs, respectively. All of the spectra have been pre- and post-edge normalized.

within the heterostructure itself. This observation therefore provides direct evidence for the presence of electron transfer occurring from $CaW_{0.2}Mo_{0.8}O_4{:}Eu^{3+}$ to either CdSe QDs or CdS QDs. In addition, we perceived that the diminution of the peak intensity near 618 eV in $CaW_{0.2}Mo_{0.8}O_4{:}Eu^{3+}$–CdSe QD composite structures is more pronounced as compared with that in analogous $CaW_{0.2}Mo_{0.8}O_4{:}Eu^{3+}$–CdS QD heterostructures.

It was also apparent that the Cd $M_{2,3}$ edge shifted to lower photon energy for the bound QDs within the heterostructure itself as compared with the signal for free QDs themselves. This observation further confirmed that the CB associated with the CdSe QDs and CdS QDs likely acts as an electron acceptor. In general, the nature of the peak shift depends on the local chemical and electronic environment of the unpaired electron. A shift to higher binding energy is suggestive of electron donation, whereas a shift to lower energy is more indicative of electron acceptor behavior.[33,75,76] In our case, the peak shift of MPA-capped CdSe QDs within $CaW_{0.2}Mo_{0.8}O_4{:}Eu^{3+}$–CdSe QD heterostructures (i.e., 619.9 eV → 618.4 eV) is larger than the analogous shift associated with comparable CdS QD-based heterostructures (i.e., 620.0 eV → 618.9 eV). These data support the idea that by comparison with CdS QDs, the CB

associated with CdSe QDs within our heterostructures can accommodate a larger number of electrons from $CaW_{0.2}Mo_{0.8}O_4$:Eu^{3+}, an assertion which is also consistent with the more prominent PEY reduction of ligand-capped CdSe QDs within our heterostructures.

Therefore, on the basis of all of our data, it is reasonable to postulate that (i) the PL quenching behavior of $CaW_{0.2}Mo_{0.8}O_4$:Eu^{3+} within both 1D $CaW_{0.2}Mo_{0.8}O_4$:(0D CdSe QD or CdS QD) composites can be ascribed to electron transfer from $CaW_{0.2}Mo_{0.8}O_4$:Eu^{3+} to either CdSe or CdS QDs and that (ii) by comparison with analogous CdS QDs, electron transfer from $CaW_{0.2}Mo_{0.8}O_4$:Eu^{3+} to MPA-capped CdSe QDs is likely to be more efficient. All of these NEXAFS findings are consistent with and corroborate the observed optical PL data, previously shown in Figure 11 and discussed in section 3.5.

4. CONCLUSIONS

We have demonstrated the first-ever ambient synthesis of both crystalline $CaMoO_4$:Eu^{3+} 1D nanowires as well as a corresponding series of crystalline, chemically well-defined solid-solutions composed of tungstate and molybdate $CaW_{1-x}Mo_xO_4$:Eu^{3+} ($0 \leq$ "x" ≤ 1) nanowires prepared under template-mediated, room temperature, aqueous conditions. The structure, morphology, crystallinity, and properties of the resulting tungstate−molybdate solid-solution nanowires have been extensively characterized and analyzed via X-ray diffraction, microscopy, and optical spectroscopy, respectively. Our as-prepared solid-solution nanowires possess average diameters of 310 ± 32 nm and lengths of 4.05 ± 1.60 μm, and we can in general control their size and morphology. Moreover, their crystallite size as well as degree of single crystallinity are unambiguously correlated and can increase with increasing Mo element ("x") in our solid-solution compounds, an observation which can be mainly attributed to the faster growth and diffusion rates of MoO_4^{2-} as compared with WO_4^{2-}.

Furthermore, as-obtained PL excitation spectra were found to gradually red-shift with increasing "x". The corresponding PL emission spectra also exhibited composition-dependent behavior. Specifically, these data highlighted efficient energy transfer from the host lattice to the Eu^{3+} activator ions, and moreover, the PL output was found to increase with higher "x" values with a maximum intensity observed with "x" = 0.8.

Moreover, we successfully have generated complex nanoscale 0D−1D heterostructures composed of either semiconducting 0D CdSe ($d \sim 2.7$ nm) or CdS QDs ($d \sim 3.5$ nm) directly coupled with 1D Eu^{3+}-activated $CaWO_4$−$CaMoO_4$ solid-solution nanowires through the mediation of organic small-molecule MPA ligands as a connecting linker. The resulting nanoscale 1D $CaW_{0.2}Mo_{0.8}O_4$:Eu^{3+} nanowire−(0D CdSe QD or CdS QD) heterostructures displayed significant PL quenching of $CaW_{0.2}Mo_{0.8}O_4$:Eu^{3+} as compared with unbound $CaW_{0.2}Mo_{0.8}O_4$:Eu^{3+} nanowires, whereas there was no apparent change in the PL properties of either CdSe QDs or CdS QDs themselves. Furthermore, the PL quenching of $CaW_{0.2}Mo_{0.8}O_4$:Eu^{3+} was more pronounced in CdSe QD-based heterostructures as compared with equivalent CdS QD-based heterostructures. We suggest that the PL quenching of $CaW_{0.2}Mo_{0.8}O_4$:Eu^{3+} can be mainly ascribed to photoexcited charge transfer occurring from $CaW_{0.2}Mo_{0.8}O_4$:Eu^{3+} to either CdSe QDs or CdS QDs.

This hypothesis has been confirmed by examining the electronic structure of the conduction band of the QDs using NEXAFS measurements. In effect, (i) the reduction in the intensity of the PEY of CdSe QDs and CdS QDs coupled with (ii) a peak shift to lower photon energy of QDs within the heterostructures as compared with unbound QDs support this idea. Overall, we propose that the composition-modulated luminescence properties over several distinctive series of as-prepared 1D tungstate-molybdate solid-solution nanowires can provide the basis for a more thorough investigation and understanding of how control over chemistry and structure can fundamentally dictate and tune related optical and optoelectronic interactions. Furthermore, probing the optical interactions within our 1D Eu^{3+}-activated tungstate−molybdate solid-solution−semiconducting nanocrystal (either CdSe or CdS QDs) heterostructures can provide a pathway toward the rational design of new types of energy-relevant architectures for possible incorporation into functional nanoscale devices. In effect, our model heterostructures offer a unique opportunity to study and explain charge and energy transfer across well-defined nanoscale interfaces.

◼ ASSOCIATED CONTENT

Ⓢ Supporting Information

Additional data on experimental setups, relevant calculations, structural characterization (including energy-dispersive X-ray spectroscopy data), as well as PL spectroscopy results on our samples. This material is available free of charge via the Internet at http://pubs.acs.org.

◼ AUTHOR INFORMATION

Corresponding Author

*E-mail: sswong@bnl.gov, stanislaus.wong@stonybrook.edu.

Notes

The authors declare no competing financial interest.

◼ ACKNOWLEDGMENTS

◼ REFERENCES

(1) Wang, Z.; Liang, H.; Wang, J.; Gong, M.; Su, Q. Red-light-emitting diodes fabricated by near-ultraviolet InGaN chips with molybdate phosphors. *Appl. Phys. Lett.* **2006**, *89* (7), 071921−071921−3.

(2) Minowa, M.; Itakura, K.; Moriyama, S.; Ootani, W. Measurement of the property of cooled lead molybdate as a scintillator. *Nucl. Instrum. Methods Phys. Res., Sect. A* **1992**, *320* (3), 500−503.

(3) Sekimoto, S.; Nakagawa, H.; Okazaki, S.; Fukuda, K.; Asakura, S.; Shigemori, T.; Takahashi, S. A fiber-optic evanescent-wave hydrogen gas sensor using palladium-supported tungsten oxide. *Sens. Actuators, B* **2000**, *66* (1), 142−145.

(4) Okazaki, S.; Nakagawa, H.; Asakura, S.; Tomiuchi, Y.; Tsuji, N.; Murayama, H.; Washiya, M. Sensing characteristics of an optical fiber sensor for hydrogen leak. *Sens. Actuators, B* **2003**, *93* (1), 142−147.

(5) Kato, A.; Oishi, S.; Shishido, T.; Yamazaki, M.; Iida, S. Evaluation of stoichiometric rare-earth molybdate and tungstate compounds as laser materials. *J. Phys. Chem. Solids* **2005**, *66* (11), 2079−2081.

(6) Poirier, G.; Jerez, V. A.; de Araújo, C. B.; Messaddeq, Y.; Ribeiro, S. J.; Poulain, M. Optical spectroscopy and frequency upconversion properties of Tm^{3+} doped tungstate fluorophosphate glasses. *J. Appl. Phys.* **2003**, *93* (3), 1493−1497.

(7) Amano, F.; Nogami, K.; Abe, R.; Ohtani, B. Preparation and characterization of bismuth tungstate polycrystalline flake-ball particles for photocatalytic reactions. *J. Phys. Chem. C* **2008**, *112* (25), 9320−9326.

(8) Liu, J.; Lian, H.; Shi, C. Improved optical photoluminescence by charge compensation in the phosphor system $CaMoO_4$:Eu^{3+}. *Opt. Mater.* **2007**, *29* (12), 1591−1594.

(9) Su, Y.; Li, L.; Li, G. Generation of tunable wavelength lights in core-shell $CaWO_4$ microspheres via co-doping with Na^+ and Ln^{3+}(Ln= Tb, Sm, Dy, Eu). *J. Mater. Chem.* **2009**, *19* (16), 2316−2322.

(10) Blasse, G.; Grabmaier, B. C. *Luminescent Materials*; Springer: Berlin, 1994.

(11) Bernard, J. E.; Zunger, A. Electronic structure of ZnS, ZnSe, ZnTe, and their pseudobinary alloys. *Phys. Rev. B* **1987**, *36* (6), 3199.

(12) Li, Y.; Zhong, H.; Li, R.; Zhou, Y.; Yang, C.; Li, Y. High-yield fabrication and electrochemical characterization of tetrapodal CdSe, CdTe, and $CdSe_xTe_{1-x}$ nanocrystals. *Adv. Funct. Mater.* **2006**, *16* (13), 1705−1716.

(13) Maeda, K.; Takata, T.; Hara, M.; Saito, N.; Inoue, Y.; Kobayashi, H.; Domen, K. GaN: ZnO solid solution as a photocatalyst for visible-light-driven overall water splitting. *J. Am. Chem. Soc.* **2005**, *127* (23), 8286−8287.

(14) Zhang, Y.; Holzwarth, N.; Williams, R. Electronic band structures of the scheelite materials $CaMoO_4$, $CaWO_4$, $PbMoO_4$, and $PbWO_4$. *Phys. Rev. B* **1998**, *57* (20), 12738.

(15) Zhang, F.; Sfeir, M. Y.; Misewich, J. A.; Wong, S. S. Room-temperature preparation, characterization, and photoluminescence measurements of solid solutions of various compositionally-defined single-crystalline alkaline-earth-metal tungstate nanorods. *Chem. Mater.* **2008**, *20* (17), 5500−5512.

(16) Han, J.; Hannah, M.; Piquette, A.; Talbot, J.; Mishra, K.; McKittrick, J. Europium activated $KSrPO_4$−$(Ba,Sr)_2SiO_4$ solid solutions as color tunable phosphors for near UV light emitting diode applications. *J. Am. Ceram. Soc.* **2013**, *96* (5), 1526−1532.

(17) Barry, T. L. Equilibria and Eu^{2+} luminescence of subsolidus phases bounded by $Ba_3MgSi_2O_8$, $Sr_3MgSi_2O_8$, and $Ca_3MgSi_2O_8$. *J. Electrochem. Soc.* **1968**, *115* (7), 733−738.

(18) Zhang, M.; Wang, J.; Zhang, Z.; Zhang, Q.; Su, Q. A tunable green alkaline-earth silicon-oxynitride solid solution $(Ca_{1-x}Sr_x)$-$Si_2O_2N_2$:Eu^{2+} and its application in LED. *Appl. Phys. B: Laser Opt.* **2008**, *93* (4), 829−835.

(19) Wu, H.; Hu, Y.; Zhang, W.; Kang, F.; Li, N.; Ju, G. Sol−gel synthesis of Eu^{3+} incorporated $CaMoO_4$: the enhanced luminescence performance. *J. Sol-Gel Sci. Technol.* **2012**, *62* (2), 227−233.

(20) Wang, Y.; Ma, J.; Tao, J.; Zhu, X.; Zhou, J.; Zhao, Z.; Xie, L.; Tian, H. Synthesis of $CaWO_4$ nanoparticles by a molten salt method. *Mater. Lett.* **2006**, *60* (2), 291−293.

(21) Lei, F.; Yan, B. Hydrothermal synthesis and luminescence of $CaMO_4$: RE^{3+} (M= W, Mo; RE= Eu, Tb) submicro-phosphors. *J. Solid State Chem.* **2008**, *181* (4), 855−862.

(22) Hou, Z.; Li, C.; Yang, J.; Lian, H.; Yang, P.; Chai, R.; Cheng, Z.; Lin, J. One-dimensional $CaWO_4$ and $CaWO_4$: Tb^{3+} nanowires and nanotubes: electrospinning preparation and luminescent properties. *J. Mater. Chem.* **2009**, *19* (18), 2737−2746.

(23) Shi, H.; Qi, L.; Ma, J.; Cheng, H. Synthesis of single crystal $BaWO_4$ nanowires in catanionic reverse micelles. *Chem. Commun.* **2002**, *16*, 1704−1705.

(24) Ho Ryu, J.; Geun Choi, B.; Yoon, J.-W.; Bo Shim, K.; Machi, K.; Hamada, K. Synthesis of $CaMoO_4$ nanoparticles by pulsed laser ablation in deionized water and optical properties. *J. Lumin.* **2007**, *124* (1), 67−70.

(25) Kim, S.-K.; Day, R. W.; Cahoon, J. F.; Kempa, T. J.; Song, K.-D.; Park, H.-G.; Lieber, C. M. Tuning light absorption in core/shell silicon nanowire photovoltaic devices through morphological design. *Nano Lett.* **2012**, *12* (9), 4971−4976.

(26) Salant, A.; Shalom, M.; Tachan, Z.; Buhbut, S.; Zaban, A.; Banin, U. Quantum rod-sensitized solar cell: nanocrystal shape effect on the photovoltaic properties. *Nano Lett.* **2012**, *12* (4), 2095−2100.

(27) McLaren, A.; Valdes-Solis, T.; Li, G.; Tsang, S. C. Shape and size effects of ZnO nanocrystals on photocatalytic activity. *J. Am. Chem. Soc.* **2009**, *131* (35), 12540−12541.

(28) Borys, N. J.; Walter, M. J.; Huang, J.; Talapin, D. V.; Lupton, J. M. The role of particle morphology in interfacial energy transfer in CdSe/CdS heterostructure nanocrystals. *Science* **2010**, *330* (6009), 1371−1374.

(29) Han, J.; Wang, L.; Wong, S. S. Observation of photoinduced charge transfer in novel luminescent CdSe quantum dot−$CePO_4$:Tb metal oxide nanowire composite heterostructures. *J. Phys. Chem. C* **2014**, *118* (11), 5671−5682.

(30) Han, J.; Wang, L.; Wong, S. S. Morphology and dopant-dependent optical characteristics of novel composite 1D and 3D-based heterostructures of CdSe nanocrystals and $LaPO_4$:Re (Re = Eu, Ce, Tb) metal phosphate nanowires. *RSC Adv.* **2014**, *4* (66), 34963−34980.

(31) Wu, Z. Y.; Ouvrard, G.; Lemaux, S.; Moreau, P.; Gressier, P.; Lemoigno, F.; Rouxel, J. Sulfur K-edge X-ray-absorption study of the charge transfer upon lithium intercalation into titanium disulfide. *Phys. Rev. Lett.* **1996**, *77* (10), 2101−2104.

(32) Chen, W.; Wang, L.; Qi, D. C.; Chen, S.; Gao, X. Y.; Wee, A. T. S. Probing the ultrafast electron transfer at the CuPc/Au(111) interface. *Appl. Phys. Lett.* **2006**, *88* (18), 184102-1−184102-3.

(33) Zhou, J. G.; Fang, H. T.; Hu, Y. F.; Sham, T. K.; Wu, C. X.; Liu, M.; Li, F. Immobilization of RuO_2 on carbon nanotube: An X-ray absorption near-edge structure study. *J. Phys. Chem. C* **2009**, *113* (24), 10747−10750.

(34) Qu, L.; Peng, X. Control of photoluminescence properties of CdSe nanocrystals in growth. *J. Am. Chem. Soc.* **2002**, *124* (9), 2049−2055.

(35) Cao, Y. C.; Wang, J. One-pot synthesis of high-quality zinc-blende CdS nanocrystals. *J. Am. Chem. Soc.* **2004**, *126* (44), 14336−14337.

(36) Robel, I.; Kuno, M.; Kamat, P. V. Size-dependent electron injection from excited CdSe quantum dots into TiO_2 nanoparticles. *J. Am. Chem. Soc.* **2007**, *129* (14), 4136−4137.

(37) Robel, I.; Subramanian, V.; Kuno, M.; Kamat, P. V. Quantum dot solar cells. Harvesting light energy with CdSe nanocrystals molecularly linked to mesoscopic TiO_2 films. *J. Am. Chem. Soc.* **2006**, *128* (7), 2385−2393.

(38) Leschkies, K. S.; Divakar, R.; Basu, J.; Enache-Pommer, E.; Boercker, J. E.; Carter, C. B.; Kortshagen, U. R.; Norris, D. J.; Aydil, E. S. Photosensitization of ZnO nanowires with CdSe quantum dots for photovoltaic devices. *Nano Lett.* **2007**, *7* (6), 1793−1798.

(39) Banerjee, S.; Hemraj-Benny, T.; Balasubramanian, M.; Fischer, D. A.; Misewich, J. A.; Wong, S. S. Ozonized single-walled carbon nanotubes investigated using NEXAFS spectroscopy. *Chem. Commun.* **2004**, *7*, 772−773.

(40) Banerjee, S.; Hemraj-Benny, T.; Balasubramanian, M.; Fischer, D. A.; Misewich, J. A.; Wong, S. S. Surface chemistry and structure of purified, ozonized, multiwalled carbon nanotubes probed by NEXAFS and vibrational spectroscopies. *ChemPhysChem* **2004**, *5* (9), 1416−1422.

(41) Hemraj-Benny, T.; Banerjee, S.; Sambasivan, S.; Balasubramanian, M.; Fischer, D. A.; Eres, G.; Puretzky, A. A.; Geohegan, D. B.; Lowndes, D. H.; Han, W. Near edge X-ray absorption fine structure spectroscopy as a tool for investigating nanomaterials. *Small* **2006**, *2* (1), 26−35.

(42) Banerjee, S.; Hemraj-Benny, T.; Sambasivan, S.; Fischer, D. A.; Misewich, J. A.; Wong, S. S. Near-edge X-ray absorption fine structure investigations of order in carbon nanotube-based systems. *J. Phys. Chem. B* **2005**, *109* (17), 8489−8495.

(43) Hu, Y.; Zhuang, W.; Ye, H.; Wang, D.; Zhang, S.; Huang, X. A novel red phosphor for white light emitting diodes. *J. Alloys Compd.* **2005**, *390* (1–2), 226–229.

(44) Yang, Y.; Li, X.; Feng, W.; Yang, W.; Li, W.; Tao, C. Effect of surfactants on morphology and luminescent properties of Ca-MoO₄:Eu³⁺ red phosphors. *J. Alloys Compd.* **2011**, *509* (3), 845–848.

(45) Page, A. G.; Godbole, S. V.; Sastry, M. D. Electronic spectra and co-operative optical transitions in CaWO₄:Tb³⁺ single crystal. *J. Phys. Chem. Solids* **1989**, *50* (6), 571–575.

(46) Sleight, A. Accurate cell dimensions for ABO₄ molybdates and tungstates. *Acta Crystallogr., Sect. B* **1972**, *28* (10), 2899–2902.

(47) Bray, A. Theory of phase-ordering kinetics. *Adv. Phys.* **1994**, *43* (3), 357–459.

(48) Lindsay, S. *Introduction to Nanoscience*; Oxford University Press: Oxford, U.K., 2009.

(49) Gao, X. P.; Bao, J. L.; Pan, G. L.; Zhu, H. Y.; Huang, P. X.; Wu, F.; Song, D. Y. Preparation and electrochemical performance of polycrystalline and single crystalline CuO nanorods as anode materials for Li ion battery. *J. Phys. Chem. B* **2004**, *108* (18), 5547–5551.

(50) Kabalnov, A. Ostwald ripening and related phenomena. *J. Dispersion Sci. Technol.* **2001**, *22* (1), 1–12.

(51) Treadaway, M. J.; Powell, R. C. Luminescence of calcium tungstate crystals. *J. Chem. Phys.* **1974**, *61* (10), 4003–4011.

(52) Grasser, R.; Scharmann, A.; Strack, K.-R. On the intrinsic nature of the blue luminescence in CaWO₄. *J. Lumin.* **1982**, *27* (3), 263–272.

(53) Wang, F.; Wang, J.; Liu, X. Direct evidence of a surface quenching effect on size dependent luminescence of upconversion nanoparticles. *Angew. Chem.* **2010**, *122* (41), 7618–7622.

(54) Han, J. K.; Hannah, M. E.; Piquette, A.; Talbot, J. B.; Mishra, K. C.; McKittrick, J. Nano- and submicron sized europium activated silicate phosphors prepared by a modified co-precipitation method. *ECS J. Solid State Sci. Technol.* **2012**, *1* (3), R98–R102.

(55) Kang, F.; Hu, Y.; Wu, H.; Ju, G.; Mu, Z.; Li, N. Enhancement of red fluorescence and afterglow in CaWO₄:Eu³⁺ by addition of MoO₃. *Displays* **2013**, *34* (4), 334–340.

(56) Chiu, C.-H.; Wang, M.-F.; Lee, C.-S.; Chen, T.-M. Structural, spectroscopic and photoluminescence studies of LiEu (WO₄)₂₋ₓ(MoO₄)ₓ as a near-UV convertible phosphor. *J. Solid State Chem.* **2007**, *180* (2), 619–627.

(57) Lu, Z.; Wanjun, T. Synthesis and luminescence properties of Eu³⁺-activated NaLa (MoO₄)(WO₄) phosphor. *Ceram. Int.* **2012**, *38* (1), 837–840.

(58) Chiu, C.-H.; Liu, C.-H.; Huang, S.-B.; Chen, T.-M. White-light-emitting diodes using red-emitting LiEu(WO₄)₂₋ₓ(MoO₄)ₓ phosphors. *J. Electrochem. Soc.* **2007**, *154* (7), J181–J184.

(59) Zeng, Q.; He, P.; Liang, H.; Gong, M.; Su, Q. Luminescence of Eu³⁺-activated tetra-molybdate red phosphors and their application in near-UV InGaN-based LEDs. *Mater. Chem. Phys.* **2009**, *118* (1), 76–80.

(60) Neeraj, S.; Kijima, N.; Cheetham, A. Novel red phosphors for solid-state lighting: the system NaM (WO₄)₂₋ₓ(MoO₄)ₓ:Eu³⁺ (M = Gd, Y, Bi). *Chem. Phys. Lett.* **2004**, *387* (1), 2–6.

(61) Chiu, C.-H.; Liu, C.-H.; Huang, S.-B.; Chen, T.-M. Synthesis and luminescence properties of intensely red-emitting M₅Eu-(WO₄)₄₋ₓ(MoO₄)ₓ (M= Li, Na, K) phosphors. *J. Electrochem. Soc.* **2008**, *155* (3), J71–J78.

(62) Sivakumar, V.; Varadaraju, U. Intense red phosphor for white LEDs based on blue GaN LEDs. *J. Electrochem. Soc.* **2006**, *153* (3), H54–H57.

(63) Cowdery-Corvan, J. R.; Whitten, D. G.; McLendon, G. L. Electron transfer reactions at CdS semiconductor cluster interfaces. Adsorption and microenvironment effects on oxidative reactions. *Chem. Phys.* **1993**, *176* (2–3), 377–386.

(64) Zhang, J. Z. Interfacial charge carrier dynamics of colloidal semiconductor nanoparticles. *J. Phys. Chem. B* **2000**, *104* (31), 7239–7253.

(65) Longo, V. M.; Gracia, L.; Stroppa, D. G.; Cavalcante, L. S.; Orlandi, M.; Ramirez, A. J.; Leite, E. R.; Andrés, J.; Beltrán, A.; Varela, J. A.; et al. A joint experimental and theoretical study on the nanomorphology of CaWO₄ crystals. *J. Phys. Chem. C* **2011**, *115* (41), 20113–20119.

(66) Cavalli, E.; Boutinaud, P.; Mahiou, R.; Bettinelli, M.; Dorenbos, P. Luminescence dynamics in Tb³⁺-doped CaWO₄ and CaMoO₄ crystals. *Inorg. Chem.* **2010**, *49* (11), 4916–4921.

(67) Dorenbos, P.; Krumpel, A. H.; van der Kolk, E.; Boutinaud, P.; Bettinelli, M.; Cavalli, E. Lanthanide level location in transition metal complex compounds. *Opt. Mater.* **2010**, *32* (12), 1681–1685.

(68) Mizel, A.; Cohen, M. L. Electronic energy levels in semiconductor nanocrystals: A Wannier function approach. *Phys. Rev. B* **1997**, *56* (11), 6737–6741.

(69) Marcus, R. A. On the theory of oxidation-reduction reactions involving electron transfer. V. Comparison and properties of electrochemical and chemical rate constants. *J. Phys. Chem.* **1963**, *67* (4), 853–857.

(70) Völker, J.; Zhou, X.; Ma, X.; Flessau, S.; Lin, H.; Schmittel, M.; Mews, A. Semiconductor nanocrystals with adjustable hole acceptors: Tuning the fluorescence intensity by metal–ion binding. *Angew. Chem., Int. Ed.* **2010**, *49* (38), 6865–6868.

(71) Hamad, K.; Roth, R.; Rockenberger, J.; Van Buuren, T.; Alivisatos, A. Structural disorder in colloidal InAs and CdSe nanocrystals observed by X-ray absorption near-edge spectroscopy. *Phys. Rev. Lett.* **1999**, *83* (17), 3474.

(72) Lee, J. R.; Meulenberg, R. W.; Hanif, K. M.; Mattoussi, H.; Klepeis, J. E.; Terminello, L. J.; van Buuren, T. Experimental observation of quantum confinement in the conduction band of CdSe quantum dots. *Phys. Rev. Lett.* **2007**, *98* (14), 146803.

(73) Kucheyev, S. O.; Baumann, T. F.; Sterne, P. A.; Wang, Y. M.; van Buuren, T.; Hamza, A. V.; Terminello, L. J.; Willey, T. M. Surface electronic states in three-dimensional SnO₂ nanostructures. *Phys. Rev. B* **2005**, *72* (3), 035404.

(74) Zhou, J. G.; Fang, H. T.; Maley, J. M.; Ko, J. Y. P.; Murphy, M.; Chu, Y.; Sammynaiken, R.; Sham, T. K. An X-ray absorption, photoemission, and Raman study of the interaction between SnO₂ nanoparticles and carbon nanotubes. *J. Phys. Chem. C* **2009**, *113* (15), 6114–6117.

(75) Annese, E.; Fujii, J.; Vobornik, I.; Rossi, G. Structure and electron states of Co-phthalocyanine interacting with the Cu(111) surface. *J. Phys. Chem. C* **2011**, *115* (35), 17409–17416.

(76) Petraki, F.; Peisert, H.; Biswas, I.; Chassé, T. Electronic structure of Co-phthalocyanine on gold investigated by photoexcited electron spectroscopies: indication of Co ion–metal interaction. *J. Phys. Chem. C* **2010**, *114* (41), 17638–17643.